Simulated and Observed Preindustrial to Modern Vegetation and Climate Changes*

MICHAEL NOTARO, ZHENGYU LIU, ROBERT GALLIMORE, STEPHEN J. VAVRUS, AND JOHN E. KUTZBACH

Center for Climatic Research, University of Wisconsin—Madison, Madison, Wisconsin

I. COLIN PRENTICE

Department of Earth Sciences, University of Bristol, Bristol, United Kingdom

ROBERT L. JACOB

Argonne National Laboratory, Chicago, Illinois

(Manuscript received 1 April 2004, in final form 27 October 2004)

ABSTRACT

Rising levels of carbon dioxide since the preindustrial era have likely contributed to an observed warming of the global surface, and observations show global greening and an expansion of boreal forests. This study reproduces observed climate and vegetation trends associated with rising CO_2 using a fully coupled atmosphere–ocean–land surface GCM with dynamic vegetation and decomposes the effects into physiological and radiative components. The simulated warming trend, strongest at high latitudes, was dominated by the radiative effect, although the physiological effect of CO_2 on vegetation (CO_2 fertilization) contributed to significant wintertime warming over northern Europe and central and eastern Asia. The net global greening of the model was primarily due to the physiological effect of increasing CO_2, while the radiative and physiological effects combined to produce a poleward expansion of the boreal forests. Observed and simulated trends in tree ring width are consistent with the enhancement of vegetation growth by the physiological effect of rising CO_2.

1. Introduction

Rising concentrations of atmospheric carbon dioxide during the twentieth century have likely contributed toward changes in both climate and vegetation. The global mean surface air temperature has risen by an estimated 0.4°–0.8°C since the late nineteenth century (Houghton et al. 2001). The warming has been most pronounced during winter and spring over the Northern Hemisphere mid- and high-latitude land, particularly 40°–70°N (Hansen et al. 1999; Houghton et al. 2001).

Consistent with the high-latitude warming of the twentieth century has been a poleward expansion of the Northern Hemisphere boreal forest (D'Arrigo et al. 1987). A greening trend in the boreal zone was identified in satellite data by Myneni et al. (1997a) and further investigated by Zhou et al. (2001) and Lucht et al. (2002). The increase in the normalized difference vegetation index (NDVI) during the 1980s and 1990s was persistent, but not homogeneous, within 40°–70°N across Eurasia and North America (Zhou et al. 2001; Tucker et al. 2001). The mid- and high-latitude greening trend is primarily a response to rising air temperatures, according to Zhou et al. (2003) and Lucht et al. (2002), and is characterized by an earlier snowmelt and spring budburst, delayed autumn leaf fall, increase in plant growth, and lengthening growing season (Myneni et al. 1997a; McCarthy et al. 2001; Lucht et al. 2002; Parmesan and Yohe 2003).

This study is the first to analyze global vegetation changes due to rising CO_2 levels from preindustrial to modern times using a fully coupled atmosphere–ocean–land model with fully interactive dynamic vegetation. Previously, Lucht et al. (2002) succeeded in reproduc-

---

* Center for Climatic Research Contribution Number 854.

Corresponding author address: Dr. Michael Notaro, Center for Climatic Research, University of Wisconsin—Madison, 1225 West Dayton Street, Madison, WI 53706.
E-mail: mnotaro@wisc.edu

ing the high northern latitude greening trend of the 1980s–1990s using the offline Lund–Potsdam–Jena (LPJ) dynamic global vegetation model (DGVM) driven by observed climate data.

Numerous studies have simulated future changes in vegetation and climate caused by the expected continuing rise in CO_2. Kicklighter et al. (1999) modeled the effects of CO_2 fertilization on terrestrial carbon from 1765 to present, and into the future, using four biosphere models. They found global increases in vegetation carbon and net primary productivity (NPP). Two earth system models of intermediate complexity were applied by Brovkin et al. (2003) to simulate rising CO_2 levels from 1800 to 2055, with results suggesting that notable atmospheric and vegetation responses to CO_2 were mostly limited to the period after 1970. A poleward expansion of the Northern Hemisphere boreal forests under $2 \times CO_2$ conditions has been simulated in several studies, using BIOME (Solomon et al. 1993; Claussen 1994; Claussen and Esch 1994; Prentice and Sykes 1995), BIOME4 (Kaplan et al. 2003), the fully coupled GENESIS Integrated Biosphere Simulator (IBIS) model (Levis et al. 2000), and the asynchronously coupled GENESIS Equilibrium Vegetation Ecology (EVE) model (Bergengren et al. 2001).

In several modeling studies, the impact of future rising CO_2 levels on vegetation has been decomposed into two components: radiative and physiological effects. Levis et al. (2000) concluded that the radiative effect produced higher temperatures and an intensified hydrological cycle, with soil moisture increasing in the midlatitudes and decreasing in the Tropics. They also found that direct physiological effects enhanced photosynthesis and weakened the hydrological cycle by reducing stomatal conductance, decreasing transpiration and precipitation, and increasing aridity in the Tropics and midlatitudes, while producing a small additional warming over the midlatitudes due to reduced evapotranspiration (Sellers et al. 1996; Betts et al. 1997; Bounoua et al. 1999). Betts et al. (2004) studied the radiative, physiological, and biogeophysical effects of rising levels of CO_2 on Amazonian forest cover and precipitation for 1860–2100 using the Hadley Centre coupled climate–carbon cycle model with dynamic vegetation. Their study mainly emphasized the future impacts of rising CO_2.

This study focuses on the preindustrial to modern period and investigates the radiative and physiological impacts of the increase in CO_2 on climate and vegetation. This period has received relatively little emphasis in prior studies. Myneni et al. (1997a) concluded from satellite data that photosynthetic activity increased 10%–12% between 45° and 70°N during 1981–91, primarily due to greater springtime warming. Fung (1997) argued that the 4% increase in CO_2 levels during this interval was insufficient to significantly enhance photosynthesis. Fung instead proposed that increasing temperatures might have accelerated snowmelt and lengthened the growing season, thereby enhancing photosynthesis, while the melting of permafrost might have released trapped nutrients. Lucht et al. (2002) concluded that the direct physiological effect of increased CO_2 contributed minimally toward the high-latitude greening trend during the satellite period. However, their simulation used the offline LPJ-DGVM driven by observed climate and therefore did not consider the possible role of biosphere–atmosphere feedbacks in producing the observed climate. The present study uses a fully coupled climate–vegetation model that allows changes in stomatal conductance, albedo, and surface roughness to influence the climate via their effects on surface fluxes of heat, water, and momentum.

Tree ring records at globally scattered sites suggest that tree growth rates have increased since the mid-nineteenth century, even prior to the warming of the twentieth century (Briffa et al. 1998). While the radiative effect of increasing CO_2 likely dominated in the twentieth century, it is also plausible that the direct CO_2 fertilization may have played a role since the mid-nineteenth century. Earlier smaller-scale studies of tree ring data, such as LaMarche et al. (1984) and Graumlich (1991), have debated the role of CO_2 fertilization in accounting for observed growth trends. The present study investigates the possible role of CO_2 fertilization during the nineteenth and twentieth centuries using observed and modeled tree ring width trends.

Section 2 describes the model, datasets, and simulations performed in this study. In section 3, the simulated vegetation is assessed against satellite-based observations with regard to biome distribution, mean vegetation cover, and seasonal cycle. Simulated and observed changes in climate are described in section 4 and vegetation in section 5, with particular focus on the northern high latitudes.

2. Description of model and data

a. Model

The model used in this study is the fully coupled global atmosphere–ocean–land Fast Ocean Atmosphere Model (FOAM)-LPJ, developed through a collaboration between the Argonne National Laboratory, the Max-Planck-Institute for Biogeochemistry, and the University of Wisconsin—Madison Center for Climatic Research (Gallimore et al. 2004, manuscript submitted to *Climate Dyn.*, hereafter GJK). The coupled atmo-

TABLE 1. List of the nine plant function types used in FOAM-LPJ.

1	Tropical broadleaved evergreen tree
2	Tropical broadleaved raingreen tree
3	Temperate needleleaved evergreen tree
4	Temperate broadleaved evergreen tree
5	Temperate broadleaved summergreen tree
6	Boreal needleleaved evergreen tree
7	Boreal summergreen tree
8	C3 grass
9	C4 grass

spheric–oceanic component is FOAM, version 1.5, an updated version of FOAM 1.0 (Jacob 1997). The atmospheric component, Parallel Community Climate Model Version 3 (PCCM3), is a parallel version of the National Center for Atmospheric Research's (NCAR's) Community Climate Model (CCM2; Drake et al. 1995), which has been updated with CCM3.6 atmospheric physics (Kiehl et al. 1998) and uses a horizontal resolution of R15 and 18 vertical sigma levels. The oceanic component, Ocean Model Version 3 (OM3), is a z-coordinate ocean model with a horizontal resolution of 1.4° latitude × 2.8° longitude, 24 vertical levels, and an explicit free surface. FOAM is highly efficient on parallel computing systems (Jacob et al. 2001), successfully captures the key observed climate features (Jacob 1997; Wu et al. 2003; Harrison et al. 2003), and produces a steady long-term climate without use of flux adjustment (Wu et al. 2003).

In FOAM-LPJ, FOAM1.5's land surface model is augmented with a modified version of the LPJ dynamic vegetation model (Sitch 2000; Cramer et al. 2001; McGuire et al. 2001; Sitch et al. 2003). The vegetation component shares the same 1.4° × 2.8° grid as the ocean component and therefore has a much higher resolution than the coarse atmospheric component of FOAM-LPJ. The specifications of the coupling of FOAM and LPJ are presented by GJK. LPJ characterizes vegetation cover per grid cell in terms of fractional cover of nine plant functional types (e.g., tropical broadleaved raingreen tree, boreal needleleaved evergreen tree, and C3 grass; see Table 1). LPJ accounts for plant competition for resources (light and water), biomass allocation for roots/stems/leaves, establishment, mortality, soil carbon and litter dynamics, and disturbances (fire) and thus determines successional vegetation changes and structure (e.g., shifts in forest/tundra and grass/desert). Figure 1 is a schematic of subdaily, daily, and annual processes in FOAM-LPJ.

b. Datasets

The mean vegetation patterns produced by FOAM-LPJ were evaluated against the Global Potential Vegetation dataset (Ramankutty and Foley 1999), consisting of 15 major vegetation types on a 0.5° × 0.5° grid, as part of the International Satellite Land Surface Climatology Project Initiative II (ISLSCP II). Potential natural vegetation represents the global vegetation cover as expected in equilibrium with the current climate and natural disturbances in the absence of human interference. The vegetation was also evaluated using the Global Continuous Fields of Vegetation Cover dataset (DeFries et al. 1999, 2000) for 1992–93 on a 1° × 1° ISLSCP II grid. This dataset gives percent coverage by trees, subdivided based on leaf longevity (evergreen and deciduous) and morphology (broadleaf and needleleaf), and grasses.

Monthly NDVI data on a 1° × 1° grid were retrieved for 1981–2001 from the National Aeronautics and Space Administration (NASA) Goddard Institute for Space Studies (GISS) and also as Fourier-adjusted, sensor and solar zenith angle corrected, interpolated, reconstructed (FASIR) NDVI for 1982–90 from ISLSCP II (Los et al. 2000). Monthly Fraction of Photosynthetic Active Radiation (FPAR) data, calculated based on NDVI, was also used for model evaluation and vegetation trend analysis. The FPAR data for ISLSCP II (Los et al. 2000) covered the period from 1982 to 1990 on a 1° × 1° grid, while Pathfinder Version 3 Advanced Very High Resolution Radiometer (AVHRR) FPAR data (Myneni et al. 1997b) extended from 1981 to 2001 on a 0.5° × 0.5° grid.

The History Database of the Global Environment (HYDE) dataset of global historical land cover (Goldewijk 2001; Goldewijk and Battjes 1997) for 1900 and 1990 on a 0.5° × 0.5° grid was used to identify regions that have been anthropogenically altered by use as croplands or pastures. To study vegetation trends prior to the satellite era, time series of tree ring width were produced from the International Tree Ring Data Bank (NOAA 1997) maintained by the NOAA Paleoclimatology Program and the World Data Center for Paleoclimatology. The data selected here covered 212 sites during 1800–1999 (most to 1990) within the band of 45°–75°N and elevations under 500 m, standardized to correct for the natural life stages of growth and decay in trees.

The (National Centers for Environmental Prediction) NCEP–NCAR reanalysis (Kalnay et al. 1996) was used to provide monthly surface air temperature data. Global air temperature trends for 1900–99 were obtained from the NASA GISS land–ocean surface air temperature anomalies dataset, which is based on a dense meteorological station network (Hansen et al. 1999) and satellite-derived SSTs (Reynolds and Smith 1994; Smith et al. 1996). Gridded monthly air tempera-

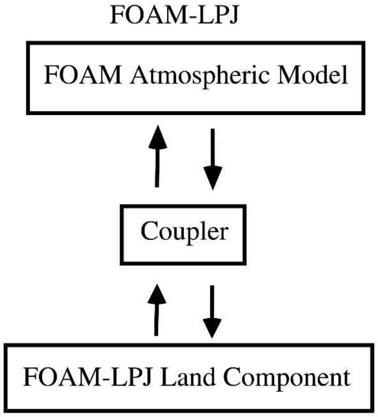

Time Stepping Calculations

Sub-daily	Daily	Annual
(1) FOAM based surface fluxes, no explicit canopy component (2) LPJ evapotranspiration (3) Surface albedo calculation based on LPJ PFT canopy structure (4) FOAM soil temperature and snow depth calculations, including canopy influence (5) Compute daily means for LPJ calculations (e.g. net solar flux at surface, surface temperature, precipitation, evapotranspiration, snowfall, snow melt)	LPJ calculations (once/day) (1) LPJ 2-layer soil water calculation (2) LPJ leaf phenology (leaf on/off) (3) LPJ canopy conductance and photosynthesis (4) LPJ daily gross primary production (5) LPJ daily respiration (6) Monthly averages (surface temperature, soil water) (7) Annual averages (precipitation, net primary production for biomass) (8) Annual sum of firelength (calculated monthly)	LPJ calculations (once/year) (1) Bioclim — determines PFT survival, establishment (true/false) (2) Reproduction — change biomass with reproductive costs (3) Turnover — leaf & root carbon to litter, sapwood to heartwood (4) Littersom — update litter pools (5) Kill — PFT death if net biomass < 0 (6) Allocation — allocate positive change biomass to stem, root, and leaves (7) Light — competition between trees and grass for space (8) Mortality — tree background and boreal heat stress mortality (9) Fire — biomass and litter destruction by fire (10) Establishment — establish (true) saplings for tree PFT's, grass to bare land, removal of PFT's not adapted to current climate (survive=false), final update of PFT grid coverage and PFT structure

FIG. 1. Schematic of subdaily, daily, and annual FOAM-LPJ processes.

ture anomalies over land on a 5° × 5° grid were obtained for 1851–2003 from the Climatic Research Unit's Land Temperatures Version 2 (CRUTEM2) dataset (Jones and Moberg 2003), based on over 3000 stations. The FOAM-LPJ simulations were compared to other models that simulated the climate response to a rise in greenhouse gases and are available from the Intergovernmental Panel on Climate Change (IPCC) Data Distribution Center for 1851–present. Global mean surface air temperature anomalies, with a base period of 1961–90, were retrieved for the following six models: Japan's Center for Climate Research Studies (CCSR), NCAR's Department of Energy Parallel Climate Model (DOE-PCM), Hadley Centre's Second Ocean–Atmosphere GCM (HadCM2), Max-Planck's ECHAM4, Australia's Commonwealth Scientific and Industrial Research Organisation Mark-2 Model (CSIRO-MK2), and Canada's first-generation Coupled Global Climate Model (CGCM1). Observed trends in global annual SST were determined using NOAA Extended Reconstruction SST (ERSST) data for 1900–99 on a 2° × 2° grid (Smith and Reynolds 2003).

The Xie–Arkin Climate Prediction Center (CPC) Merged Analysis of Precipitation dataset (Xie and Arkin 1996, 1997) was the source of monthly 2.5° × 2.5° precipitation data for 1979–2001. The Willmott–Matsuura V1.01 temperature and precipitation data [Willmott and Matsuura 2000; obtained from NOAA–Cooperative Institute for Research in Environmental Sciences (CIRES) Climate Diagnostics Center] provided gridded precipitation data on a 0.5° × 0.5° grid for 1950–96. The Climatic Research Unit's Time Series

TABLE 2. Outline of model simulations. Details include the simulation name, a brief description, run length, and the concentrations of CO_2 used in the atmospheric and biosphere components of the model.

Simulation	Description	Run length (yr)	Atmospheric CO_2 (ppmv)	Vegetation CO_2 (ppmv)
PIC	Preindustrial control	400	280	280
MOC	1975 (modern) control	200	335	335
FC	1975 flux-adjusted control	100	335	335
RP	Radiative + physiological	100	280 to 433 equivalence	280 to 370
R	Radiative	100	280 to 433 equivalence	280
P	Physiological	100	280	280 to 370

Data Version 2.0 (CRU TS2.0) dataset provided observed land surface precipitation data for 1901–2000.

c. *Model simulations*

Several control and transient model simulations were produced with FOAM-LPJ (Table 2). No relaxation or correction of climate forcing toward observed values was applied to adjust the simulated vegetation. The preindustrial control (PIC) run consisted of 400 years with the atmosphere, ocean, and vegetation in equilibrium and a CO_2 concentration of 280 ppm, following a 420-yr spinup period that started from bare ground (GJK). The "modern" control (MOC) run, initiated from the end of the PIC run, consisted of 200 equilibrium years with a CO_2 concentration of 335 ppm (1975 level). The radiative and physiological (RP) effects of rising CO_2 levels were examined by a three-member ensemble, compressing the CO_2 increase from preindustrial (1800) to modern times (2000) into 100 years of simulation. In FOAM-LPJ, the CO_2 level used for photosynthesis in the vegetation model (physiological value) can be set separately from the value used in the atmospheric model (radiative value). In the RP runs, the physiological CO_2 value was increased from 280 to 370 ppm, while the radiative value (equivalent CO_2) was increased from 280 to 433 ppm to account for both CO_2 and additional trace gases that do not have physiological effects. The radiative-only effect was examined in run R by increasing the radiative value from 280 to 433 ppm while maintaining the physiological value at 280 ppm. The physiological-only effect was assessed in run P, where the radiative value was held at 280 ppmv while the physiological value was increased from 280 to 370 ppm. Cases RP, R, and P were all 100-yr transient simulations, initiated from the end of the PIC run. Finally, a flux-corrected (FC) simulation was performed as a 100-yr flux-corrected control with 1975 CO_2 levels. Surface air temperature and precipitation input to the LPJ component was flux adjusted against the NCEP–NCAR reanalysis and Xie–Arkin precipitation, respectively, in run FC only.

3. Model evaluation

a. *Biomes*

The biome distribution simulated by the fully coupled FOAM-LPJ control run MOC was compared with that of potential natural vegetation (PNV) (Ramankutty and Foley 1999), as shown in Fig. 2. For comparison purposes, the 15 vegetation categories of PNV and 9 vegetation categories of FOAM-LPJ were merged into seven major biomes: tropical forest, temperature forest, boreal forest, savanna and dry woodland, dry grassland and shrubland, desert, and tundra. The simulated biomes were determined from the FOAM-LPJ output using tree cover, vegetation cover, canopy height, and growing degree days (GDDs) based on an algorithm outlined in Fig. 11 of Joos et al.(2004). The comparison is approximate (because of differences in biome definitions between the dataset and the model) but nonetheless informative. The control run was successful in reproducing major ecosystems of the world, including the Sahara, Arabian, and central Asian Deserts; rainforests in the Amazon, Congo, Central America, and Southeast Asia; the boreal forests of Canada, Alaska, and northern Eurasia; and the polar tundra. At higher latitudes, the North American boreal forest was particularly well simulated. One general model bias is the overproduction of forest biomes. Wet biases (Fig. 3), clearly seen in the comparison of model precipitation with Xie–Arkin precipitation data, result in the production of temperate forests in the central United States and Australia (where dry grassland and shrubland exist), an overextended African rainforest, boreal forest unrealistically extended over northern China and Mongolia, and too little dry grassland and shrubland at a global scale. Tree cover, however, was undersimulated over the northeastern Amazon and New Guinea due to dry biases in these limited regions. A persistent cold bias in the northern high latitudes led to a southward displacement of the Eurasian boreal forest and overextensive tundra and polar desert. The tendency for the model to produce more tree and less

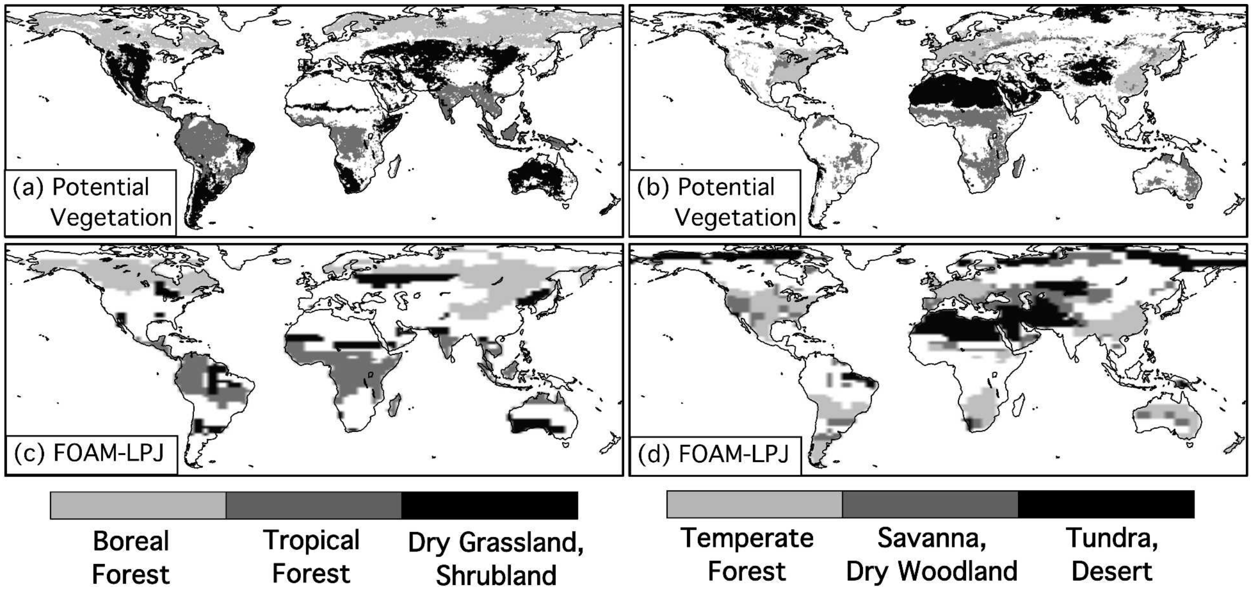

FIG. 2. (a) Potential vegetation (Ramankutty and Foley 1999) biome map for boreal forest, tropical forest, and dry grassland/shrubland. (b) Potential vegetation biome map for temperate forest, savanna/dry woodland, and tundra/desert. (c) As in (a) but based on 150 years of FOAM-LPJ's MOC run. (d) As in (b) but for FOAM-LPJ.

grass cover than observed is partly due to its overactive hydrological cycle, which in the net contributes an overabundant supply of soil water available for tree growth and partly to a general woody bias in LPJ (Sitch et al. 2003).

Figure 4 compares the percent tree cover from the last 150 years of the MOC control run and the observed 1992–93 coverage from Global Continuous Fields of Vegetation Data (DeFries et al. 1999, 2000). The distribution of simulated and observed global tree cover are spatially correlated at $r = 0.56$; the model's tendency to overproduce tree cover is reflected by a root-mean-square error (rmse) of 53%. Errors in simulated vegetation were partly due to model precipitation and temperature biases, as no attempts were made to flux correct the climate. The overabundance of simulated tree cover over the U.S. Great Plains, China, Sahel, South Africa, and Australia can be primarily attributed to local FOAM wet biases. However, as evident through HYDE data (Goldewijk 2001), land use has altered natural vegetation cover over these same regions (Fig. 4), so some model−observed differences and a portion of the high rmse could be due to the absence of land use in the model.

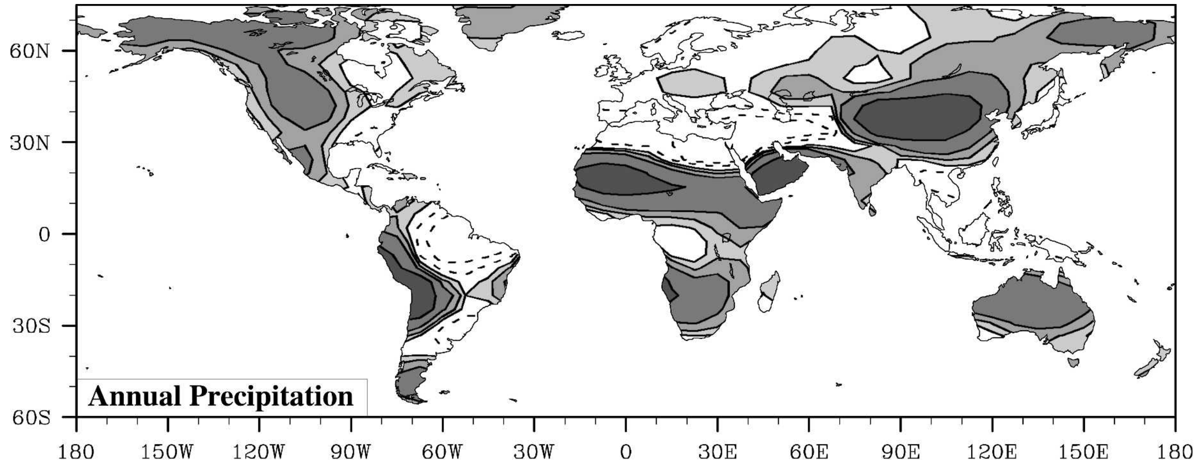

FIG. 3. Smoothed percent difference (model–observed) in annual average land precipitation over land between the MOC control and 1979–2001 Xie–Arkin data. Contours include 20%, 50%, 100%, and 300%, with differences exceeding +20% in different gray shades.

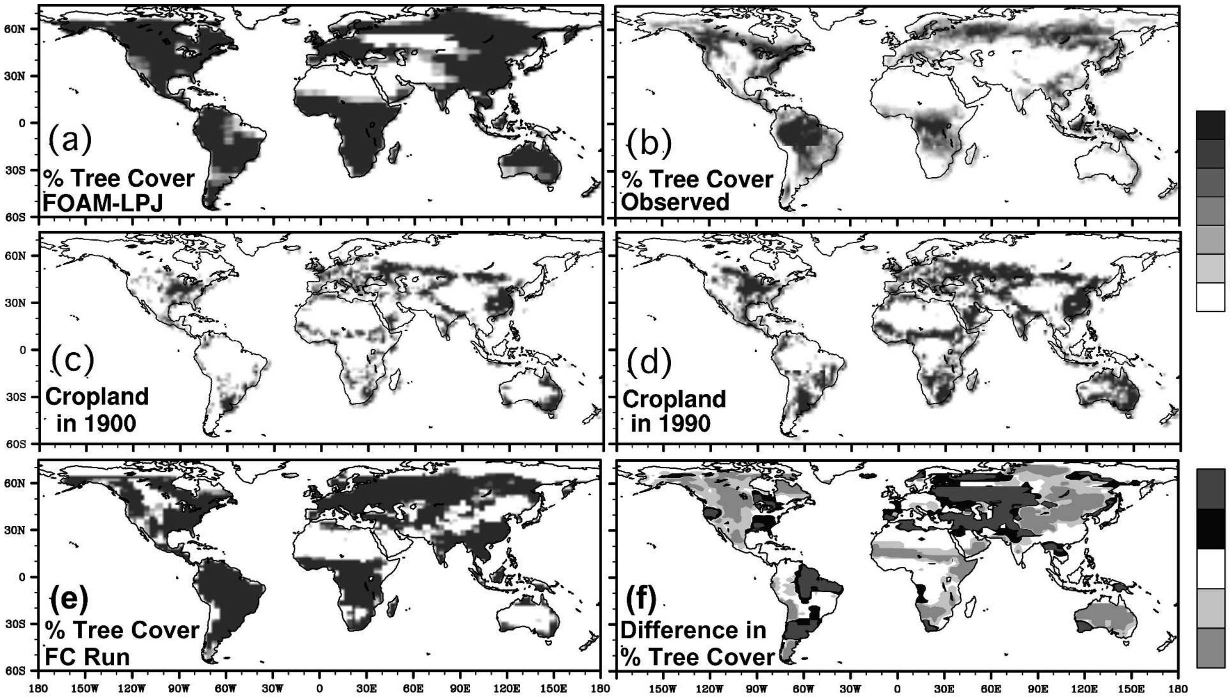

FIG. 4. (a) Average percent tree cover in the last 150 years of MOC control. (b) Observed 1992–93 percent tree cover from Global Continuous Fields of Vegetation Data (DeFries et al. 1999, 2000). (c) Regions covered by cropland in 1900, based on HYDE data (Goldewijk 2001). (d) As in (c) but for 1990. (e) As in (a) but for flux-adjusted run FC. (f) Difference in simulated percent tree cover (FC–MOC). Upper label bar applies to (a)–(e) and lower label bar applies to (f).

The present-day simulation of the Third Hadley Center Coupled Climate-Carbon Cycle GCM (HadCM3LC) coupled climate–carbon cycle model by Betts et al. (2004) likewise contains biases based on comparison with the satellite vegetation data. Their simulation produced too much broadleaf tree cover in the Tropics and not enough in the extratropics, in addition to an excess of needleleaf tree cover over Canada and a deficit over northeast Asia and the United States. However, both the present study and that of Betts et al. (2004) captured the general observed pattern of broadleaf dominance in the Tropics and needleleaf dominance at the higher latitudes.

b. *Mean vegetation*

The comparison of model FPAR from the control run MOC and satellite-derived 1982–90 FPAR (Los et al. 2000) for January and July is shown in Fig. 5. Despite producing too much tree cover, FOAM-LPJ captures seasonal features such as the summertime greening of vegetation cover across North America and Eurasia and seasonal shifts over central and southern Africa. The mean FPAR for 60°S–75°N for the observations and model was 0.20 and 0.34 in January and 0.41 and 0.64 in July, respectively. Spatial correlations over this latitudinal band were 0.50 (significance level $P < 0.01$) in January and 0.41 ($P < 0.01$) in July. Using the global continuous fields of vegetation data (DeFries et al. 1999, 2000), correlations between observed and modeled annual percent tree cover, broadleaf tree cover, and needleleaf tree cover were 0.33 ($P < 0.01$), 0.49 ($P < 0.01$), and 0.54 ($P < 0.01$), while noting the absence of anthropogenic land use categories in the model. While total model vegetation cover averaged just 6% greater than observed (simulated 79%; observed 73%), the model produced an excess of tree cover and too little grasslands due to certain regional wet biases, the lack of incorporating anthropogenic land use, and LPJ's woody bias.

c. *Flux adjustment*

The flux-adjusted 100-yr simulation FC was performed as a sensitivity experiment for comparison with control run MOC. Global precipitation rates over land averaged 2.52 and 1.84 mm day^{-1} in run MOC and Xie–Arkin data, respectively, with FOAM-LPJ simulating 37% greater precipitation than observed. The coarse topography used by R15 FOAM greatly underestimated the peaks of the Rockies, Andes, and Tibetan Plateau by as much as 1–2 km, likely contributing toward regional wet, woody biases over and downstream

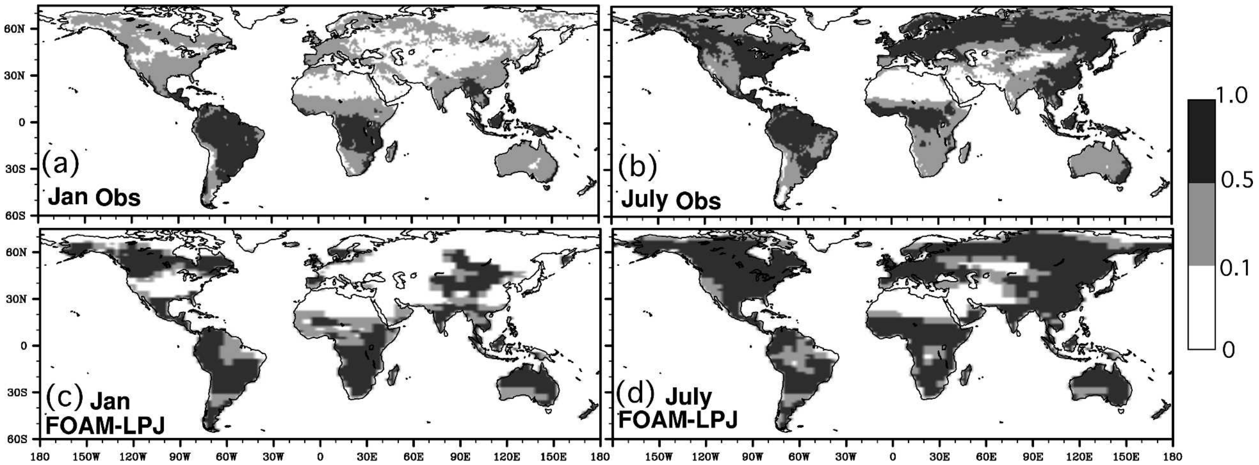

FIG. 5. Satellite-derived average FPAR (Los et al. 2000) for (a) Jan and (b) Jul and model-calculated average FPAR for (c) Jan and (d) Jul based on 150 years of the MOC run. Values less than 0.1 are not shown.

of the mountains (e.g., U.S. Great Plains and China). Over Africa, the simulated ITCZ shows too large a seasonal shift, resulting in a wet, woody bias over the southern Sahara and southern Africa. The model also pushed the ITCZ too far south into Australia in austral summer, producing a wet, woody bias. A few regions did exhibit dry, low vegetation biases, such as northern Brazil (due to simulated cool Atlantic SSTs) and the Middle East. The control simulation also exhibited a large cold bias during boreal winter and spring over Europe and northern Asia.

The inclusion of flux adjustment to temperature and precipitation in run FC produced a decrease in tree cover by 5% and grass cover by 3% globally. Specifically, vegetation cover was reduced over the U.S. Great Plains, Australia, the southern Sahara, southern Africa, the Horn of Africa, Canada, and northwest China and increased over northern Brazil, Argentina, and eastern Europe (Fig. 4). In run FC, FOAM-LPJ simulated reasonably well the Australian, Kalahari, Arabian, Atacama, and Patagonian Deserts, while also reducing tree cover in the Great Plains and correctly positioning the Sahel's forest–desert gradient. However, LPJ continued to exhibit a woody bias even in the flux-adjusted simulation FC. Sitch et al. (2003) found that LPJ, when forced with observational data, produced a reasonable simulation of tropical, temperature, and boreal forests and grasslands but overproduced forest cover and underproduced grass cover.

Flux adjustment can distort climate sensitivity (Fanning and Weaver 1997; Gregory and Mitchell 1997) and variability, disguises systematic model errors, and is not based on physical climate processes. Given the absence of drift on the century time scale and continuing work to improve the coupled model, we chose to work principally with FOAM-LPJ transient simulations without flux adjustment.

4. Changes in climate

Due to complex feedbacks between the atmosphere and land surface, it can be challenging to determine causal mechanisms behind trends in climate and vegetation. For the purpose of organization, changes in observed and simulated climate will be discussed first (section 4), followed by an analysis of vegetation changes (section 5).

The study focuses on simulating changes in climate and vegetation due to rising levels of (equivalent) CO_2. Several studies have found that natural forcings (solar variability and volcanism) played a significant role early in the twentieth century, while greenhouse forcings became dominant late in the century (Stott et al. 2000; Tett et al. 2000; Stott et al. 2001; Meehl et al. 2003). Lucht et al. (2002) also showed, through satellite data and an LPJ simulation, that vegetation growth briefly slowed following the Pinatubo eruption.

Here, the simulations with FOAM-LPJ do not include forcings from anthropogenic land use, volcanic eruptions, aerosols, or solar activity, so it is not expected that the observed and simulated climate variations will closely match. The focus of our analysis is on the climatic and vegetative trends since preindustrial times due to rising levels of equivalent CO_2, rather than on interannual or decadal variability.

a. Global surface air temperature

The mean global surface air temperature shows a warming trend in both the model simulations and

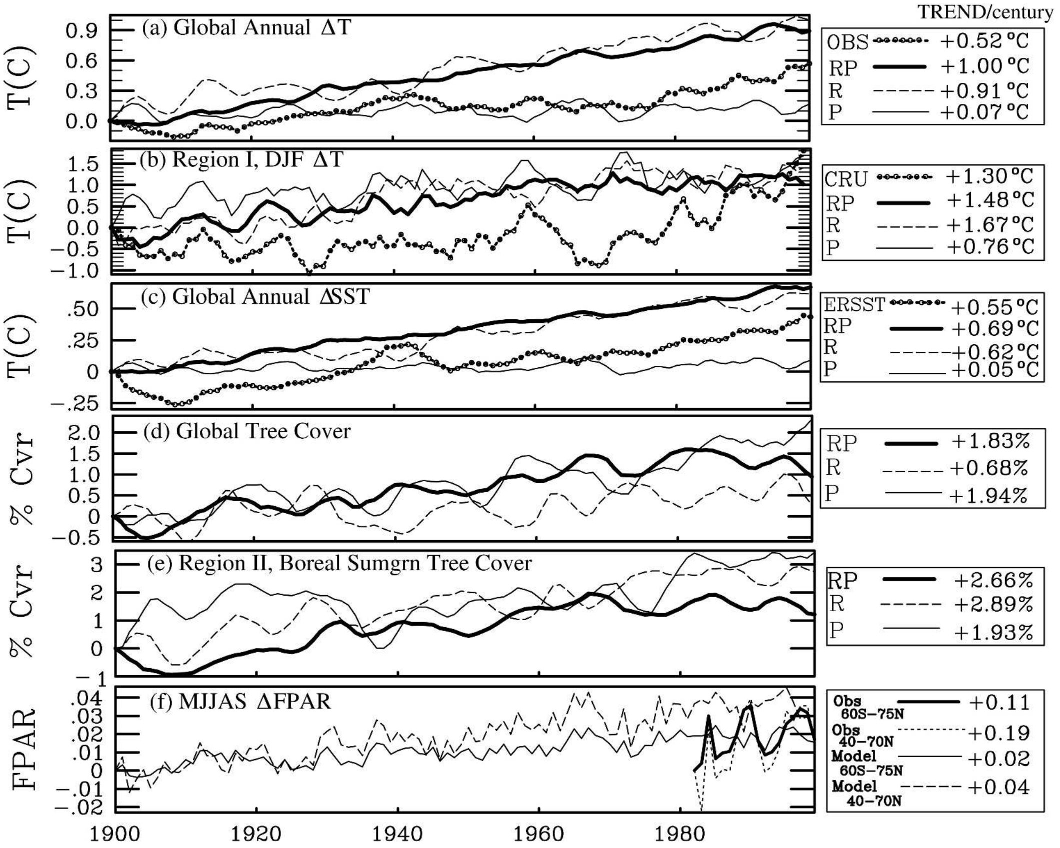

FIG. 6. Time series from 1900 to 1999 of anomalies from the first year. (a) Smoothed global mean surface air temperature anomalies (°C) from NASA GISS observations and the RP, R, and P runs. (b) Smoothed DJF surface air temperature anomalies (°C) over land within 38°–60°N, 120°W–140°E from CRU data (Jones and Moberg 2003) and the RP, R, and P runs. (c) Smoothed global annual average SST anomalies (°C) from ERSST data (Smith and Reynolds 2003) and the RP, R, and P runs. (d) Smoothed global mean percent tree cover anomalies over land from the RP, R, and P runs. (e) Smoothed boreal summergreen percent tree cover anomalies over land within 40°–75°N from the RP, R, and P runs. (f) FPAR anomalies for May–Sep from 1982 to 1999 satellite-derived data (Myneni et al. 1997b) and the RP runs.

NASA GISS observations for 1900–99 (Hansen et al. 1999; Reynolds and Smith 1994; Smith et al. 1996), as illustrated in Fig. 6a. The average trends were +0.5°, +1.0°, +0.9°, and +0.1°C century^{-1} for the observational time series and the RP, R, and P simulations, respectively. The overall warming trend in the RP ensemble was about twice that observed, perhaps partly due to the absence of other external forcing factors (e.g., volcanic activity and aerosols) in the model, or perhaps due to model bias (e.g., overactive hydrological cycle). The simulated warming trend was predominantly radiatively driven, with the physiological impact of the CO_2 increase having only a small effect on global mean temperature. Over land, the Willmott–Matsuura dataset shows a warming of 0.5°C during 1950–96, with more substantial warming in the 45°–70°N boreal band.

The warming trend produced by FOAM-LPJ is similar to six other IPCC-participating GCM simulations performed with rising greenhouse gases in the twentieth century. The six models, forced only by IS92a rising levels of greenhouse gases, warmed an average of 1.1°C, which closely matches the 1.0°C warming in the RP ensemble but exceeds the observed warming.

The spatial pattern of annual temperature change in simulation RP (not shown) generally agreed with the NCEP–NCAR reanalysis, with a spatial correlation of 0.52 ($P < 0.01$) between the model's 100-yr trend and the 1951–2000 trend from the reanalysis, and 0.36 ($P < 0.01$) between the model's and reanalysis's 1951–2000 trend. The model failed to produce any local areas of cooling over land, such as the cooling trend observed over eastern North America during 1950–96 in the Willmott–Matsuura data. The model, reanalysis, and Willmott–Matsuura data all exhibited the strongest warming across northern Asia and western Canada, approximately 1°–3°C. Both the RP and R simulations produced a general warming of 1°–3°C north of 30°N, greater at the higher northern latitudes. Overall changes in annual temperature in run P were much smaller, with a warming of about 0.4°C over Europe, central and eastern Asia, and the central United States and a broad area of cooling across Alaska and the remaining extreme Arctic latitudes. The much weaker warming trend in run P versus run R shows that the radiative effect of rising CO_2 on annual surface air temperature dominated over the physiological effect during the period from preindustrial to modern times.

In agreement with the findings of Sellers et al. (1996) and Bounoua et al. (1999), the sum of the model-simulated changes in temperature for the R [$+0.78°C\ (100\ yr)^{-1}$] and P [$+0.08°C\ (100\ yr)^{-1}$] runs closely approximated the RP ensemble [$+0.88°C\ (100\ yr)^{-1}$] across much of the lower latitudes (40°S–40°N). This additive feature was less evident in the extratropics, particularly in the northern winter and high latitudes. Sellers et al. (1996) concluded that the trends were additive in the Tropics owing to the emphasis on local processes, while nonlocal influences could produce a nonadditive effect at the northern mid and high latitudes. In the present study, the annual temperature trends were not additive in the mid and high latitudes, as suggested by Sellers et al. (1996), with $RP > R + P$ over Alaska and northern Canada, northern Europe, and far eastern Russia and $RP < R + P$ over north-central Asia. Specifically, the annual temperature trends averaged over 50°–90°N were +1.98°, +1.79°, and –0.04°C in the RP, R, and P runs, respectively. Trends in simulated annual surface air temperature for the Northern Hemisphere are presented in Fig. 7.

b. Northern winter surface air temperature

Significant wintertime warming in association with the physiological CO_2 forcing was simulated, exceeding the response of annual temperature. Simulated climate changes are described first and later related to vegetation changes, whenever possible, in section 5. Figure 8 compares the December–February (DJF) trends in surface air temperature north of 30°N in the RP, R, and P cases. The general trend features in RP and R reflect a widespread warming, strongest at high latitudes, with weak cooling only near Greenland. In run P, there are three distinct regions of warming and statistically insignificant cooling across Alaska and north of about 70°N. Over Europe, a statistically significant warming of up to $+2.0°C\ century^{-1}$ ($P < 0.05$) coincided with a deepened Icelandic low and enhanced westerlies and warm advection, although the mechanism for this is not well understood. Across central and eastern Asia, an erosion of the northern portion of the Siberian high by 1–4 hPa reduced its access to cold Arctic air and led to a statistically significant warming of up to $+1.6°C\ century^{-1}$ ($P < 0.05$). As CO_2 levels rose, the boreal needleleaf evergreen cover expanded over central Asia, supporting a weak warming, mostly by less than 0.5°C (as surface albedo decreased), and pressure drops of about 1–1.5 hPa over the Siberian high in September–November (SON) corresponding to reduced stability. By DJF, the northern Siberian high was up to 4 hPa weaker, resulting in a warming of about 1°–1.5°C and an increasing specific humidity over and to the east of the high, primarily due to reduced cold advection. The third area of DJF warming was located over central United States and averaged $+0.8°C\ century^{-1}$ (not significant). Higher total FPAR during SON over northern Europe and eastern Asia due to the physiological effect of CO_2 increase suggests a longer growing season and extended maintenance of the forest canopy, which would serve to absorb additional heat early in the winter and lower the surface albedo (reduced positive snow/albedo feedback). In all three regions, the FPAR of boreal needleleaf evergreen trees increased and supported the wintertime warming in run P.

Figure 6b presents time series of average DJF surface air temperature anomalies over land within the region of 38°–60°N, 120°W–140°E for the RP, R, and P simulations and CRU data. This region was selected to represent an area where both physiological and radiative forcings produced significant temperature trends. The respective temperature trends were +1.5, +1.7, +0.8, and +1.3 ($°C\ century^{-1}$). Correlations of the RP, P, and R time series with the CRU data are +0.59, +0.53, and +0.49, respectively. During the second half of the twentieth century, the reanalysis and Willmott–Matsuura datasets also showed enhanced warming over western Canada and northern Eurasia. The Willmott–Matsuura dataset exhibited a 1°C warming for 1950–96 over the region specified in Fig. 6b.

The northern winter trends showed more nonadditive features than did the global trends ($R + P \neq RP$). Averaged across the region specified in Fig. 6b, the R + P DJF trend ($+2.5°C\ century^{-1}$) exceeded the trend in RP ($+1.5°C\ century^{-1}$). In particular, $R + P > RP$ across the U.S. Midwest, Europe, and central Asia, while $RP > R + P$ mainly north of 70°N. The tendency of $R + P > RP$, particularly in winter, over the Eurasian and North American boreal forest in the present study agreed with the finding of Bounoua et al. (1999), who suggested that year-round physiological responses in the Tropics were impacting the northern high-latitude wintertime climate.

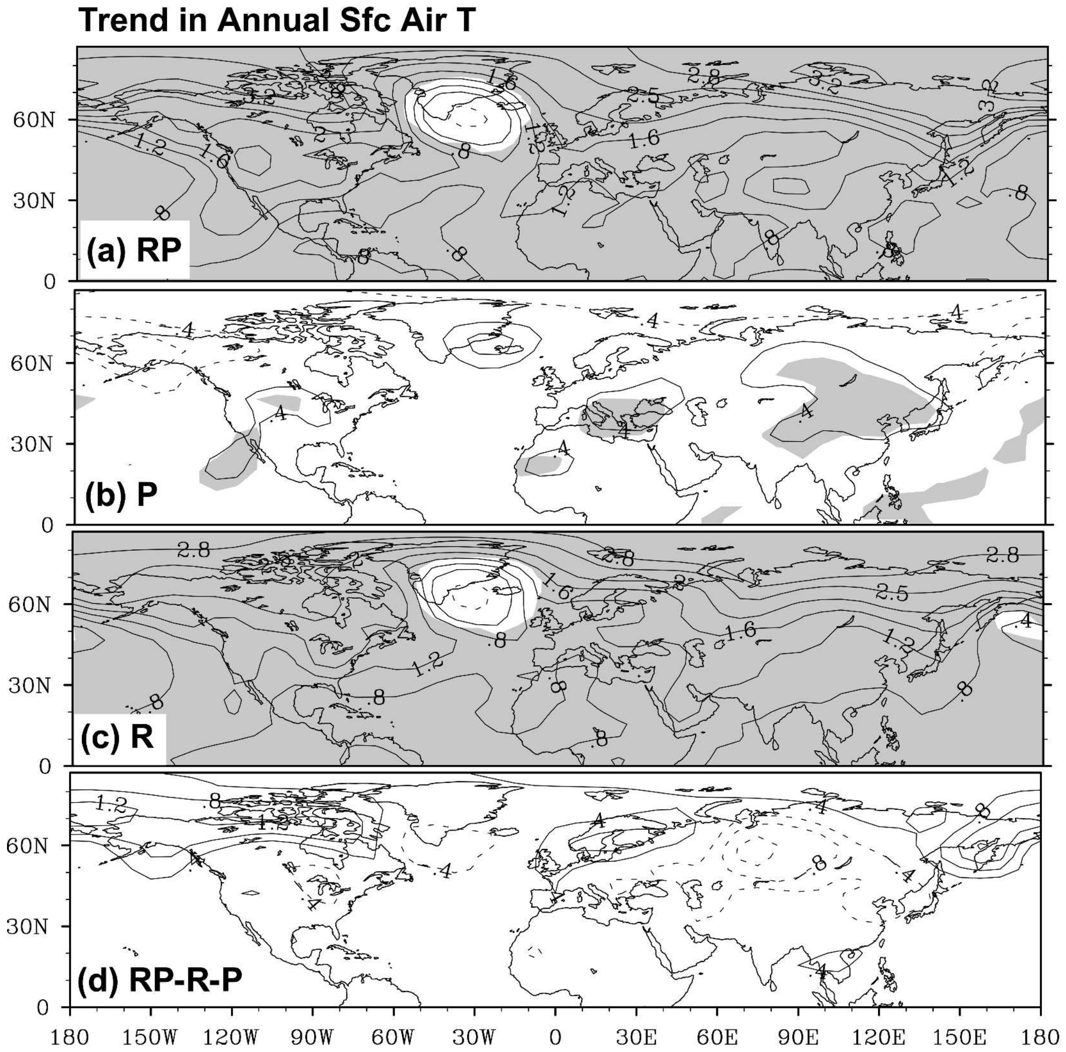

FIG. 7. Trend in annual surface air temperature (°C century^{-1}) over 100 years for the (a) RP, (b) P, and (c) R runs over the northern mid- and high latitudes. (d) The difference in trends (RP − R − P). Shading in (a)–(c) represents statistically significant trends with alpha $P < 0.05$.

Chase et al. (2001) analyzed coupled climate model simulations during the preindustrial to modern period and found that increased levels of CO_2 and sulfate aerosols resulted in a January warming of 1°–3°C over much of the northern mid- and high latitudes. The warming over the northern mid- and high latitudes in run R (without aerosols) mostly averaged 1°–4°C during boreal winter (Fig. 8). Chase et al. (2001) found that historical land cover changes in additional simulations resulted in temperature changes close in magnitude to those produced in the previously mentioned simulations. These temperature changes that resulted from land cover use were most distinct over land but also developed remotely due to changes in large-scale circulation; this was roughly analogous to the peak warming over land and additional remote changes in temperature seen in run P here.

c. Sea surface temperature

Global SST trends, shown in Fig. 6c, were +0.7, +0.6, 0.0, and +0.5 (°C century^{-1}) for the RP, R, and P runs and ERSST observations. In the RP ensemble, the largest annual SST warming, of at least +1.0°C century^{-1}, occurred around the Gulf of Alaska, extending down the west coast of North America, and off the coast of the northeastern United States. Similar to Ganopolski et al. (1998), we identified a synergy between increasing vegetation cover and SST in the Arctic. Although the mechanism is unclear, the physiological impact of rising CO_2 on SSTs was most notable during DJF along the

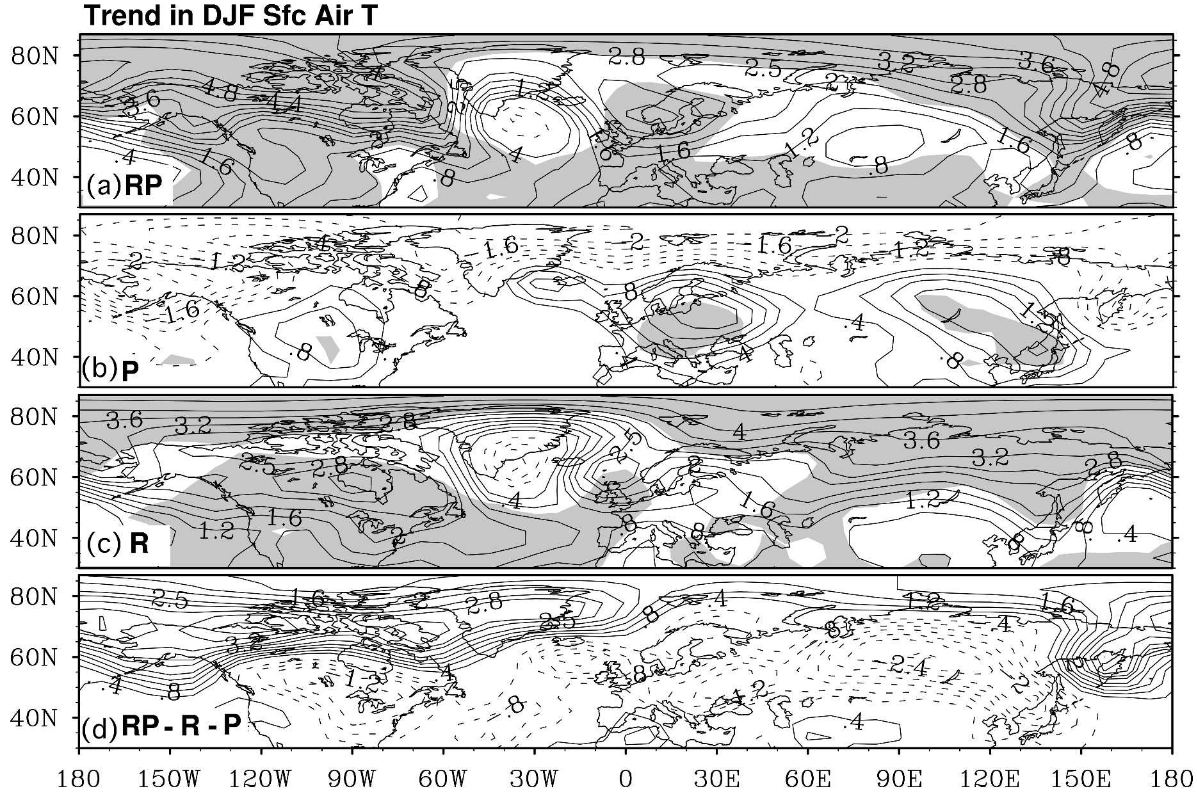

FIG. 8. As in Fig. 7 but for DJF.

west coast of North America and around Central America, with trends in magnitude up to ±1.0°C century^{-1} ($P = 0.05$).

d. Hydrological cycle

Observations suggest an increase in precipitation over Northern Hemisphere high-latitude land (Houghton et al. 2001), particularly during the cold season (Easterling et al. 2000). According to CRU TS 2.0 data for 1901–2000, land precipitation has increased globally by 2% and within 24°–90°N by 4%. However, the global increase in CRU precipitation was primarily due to an increase in the 1940s, with a slight drying trend after the 1970s. The Willmott–Matsuura data for 1950–96 contains a global drying of 1%, but a 2% increase over 24°–90°N. There were small increases in land precipitation both globally and within 24°–90°N in the RP (2%) and R (1%) runs, while no overall trend in annual precipitation was identified in run P. This suggests a possible link in global precipitation rise to the radiative effect of increased CO_2. Increased precipitation and soil moisture in the RP ensemble occurred across northern Eurasia and much of the United States in association with positive FPAR trends. The spatial agreement between observed and simulated precipitation trends was less than for temperature, probably due to the spatial complexity of precipitation patterns and the absence of anthropogenic land use in the model, which can greatly impact the local hydrological cycle. One feature common to the RP, R, and P runs, which disagreed with the 1980–2000 Xie–Arkin and 1951–2000 reanalysis data, was an increase in tropical North Pacific precipitation, about 0.1–0.5 mm day^{-1} century^{-1}. In the RP ensemble, Indonesian precipitation increased about 20% century^{-1} as the model cold tongue retreated eastward. Despite the absence of a global change in precipitation in run P, a decreasing trend was noted over the Congo and southern Amazon tropical forests, coinciding with decreases in evapotranspiration and surface specific humidity. It is likely that the physiological forcing reduced stomatal conductance, thereby reducing moisture recycling, consistent with Betts et al. (2004) and Levis et al. (2000).

A 3% increase in evapotranspiration was noted in the RP ensemble, amplifying the smaller 1% increase in the other two runs. The radiative effect of rising CO_2 levels led to a 3% decrease in tropical land evapotranspiration, particularly over the Amazon and Congo, where mean FPAR, precipitation, and soil moisture also diminished due to weakened moisture recycling. Within 24°–90°N, evapotranspiration increased by 8%, 6%, and 1% in the RP, R, and P runs, respectively. Increases in both evapotranspiration and FPAR were produced over northern high-latitude Asia in the R and RP runs, as warming temperatures allowed for an increase in plant growth. The physiological effect of rising CO_2 caused an increase in evapotranspiration and summertime FPAR over northern Mexico, northern Russia, and southern Asia. Positive FPAR trends in run P over regions of low vegetation cover and moisture availability (e.g., North Africa, northern Brazil, the U.S. Southwest and northern Mexico, central Asia, and northern tundra) resulted in locally enhanced evapotranspiration and precipitation. Global land surface evaporation increased 1% in the RP ensemble and even less in the R and P runs. Within 24°–90°N, land surface evapotranspiration increased by 2% in the RP and R runs, with an even smaller increase in run P. Globally, in the RP ensemble, precipitation over land increased at a greater rate than evaporation (*P:* +1.6%; *E*: +0.5%), while evaporation over the ocean increased at a greater rate than precipitation (*P*: +1.0%; *E*: +1.4%). The resulting 2% increase in freshwater runoff into the ocean, along with melting of sea ice, likely contributed to a weakening of the thermohaline circulation. The mean meridional overturning substantially weakened in the RP runs up to 20%–30% in both the North Atlantic and Pacific and up to 5%–10% in both the South Atlantic and Pacific.

Surface specific humidity increased worldwide in the RP and R simulations, particularly over the Tropics, in association with the rise in global precipitation. Houghton et al. (1995) also reported a rise in observed atmospheric water vapor in the Tropics since 1973. Increases of $+0.8\ \mathrm{g\ kg^{-1}\ century^{-1}}$ extended from the north Indian Ocean across the tropical Pacific. Trends in specific humidity were weaker and varied in sign in the physiological run P. Surface moisture increased by 0.1–0.4 $\mathrm{g\ kg^{-1}\ century^{-1}}$ over southern and southeastern Asia and also across the tropical North Pacific, extending into northern Mexico and the southern United States, in association with the increased precipitation in both regions. Positive trends in soil moisture in the RP runs were simulated over northern Asia and Canada, coinciding with enhanced warming and FPAR.

5. Changes in vegetation

Observed and simulated trends in vegetation will now be related to the previously discussed changes in climate.

a. Modeled and observed vegetation trends

Satellite data of NDVI and FPAR during the 1980s and 1990s reveal a greening trend, particularly in the boreal zone (where land use is a minor factor), although the temporal duration of the data is limited and there is large interannual variability. It is therefore of interest to examine this trend using a fully coupled model. The transient simulations in this study serve to investigate how natural global vegetation, particularly boreal vegetation, might have varied during the twentieth century as a result of the various effects of increasing CO_2.

The physiological effect appeared dominant over the radiative in global changes in vegetation amount. Global mean tree cover over landmasses increased by 1.8, 0.7, and 1.9 ($\%\ \mathrm{century^{-1}}$) for the RP, R, and P simulations (Fig. 6d). Each individual ensemble member of RP produced similar results, with total changes in global forest cover fraction of $+1.7 \pm 0.6\%$, greater than twice the standard deviation in global forest cover. As evidence of global greening, global mean vegetation cover over land also increased about 2.4% in RP and 2.1% in P, both greater than the 0.8% increase in run R. Total forest biome coverage within 30°–90°N increased from 2.73 to 2.82 ($\times 10^7\ \mathrm{km^2}$) (+3.3%) in the RP ensemble, while the area of polar desert, tundra, and forest tundra biomes (excluding Greenland) diminished from 1.42 to 1.20 ($\times 10^7\ \mathrm{km^2}$) (−15.2%).

Enhancement of tree cover was almost exclusively limited to the northern high latitudes in the radiative simulation R, whereas in the physiological simulation P, there were notable increases in boreal summergreen, boreal needleleaved evergreen, and temperate broadleaved evergreen tree cover over broad areas. Despite the small increase in CO_2, the global mean tree cover began increasing in run P during the first two decades. In run R, there was a general increase in deciduous tree cover, mainly boreal summergreen and tropical broadleaved raingreen, largely due to a lengthening growing season and a decrease in evergreen tree cover, mainly boreal needleleaved evergreen. Within 40°–75°N, boreal summergreen tree cover over land increased at +2.7, +2.9, and +1.9 ($\%\ \mathrm{century^{-1}}$) for runs RP, R, and P, respectively, illustrating the importance of both the radiative and physiological effects in the boreal greening (Fig. 6e). In both the observed 1982–99 FPAR data and 100-yr RP simulations, FPAR for May–September increased by 0.02 over 60°S–75°N (globe) and by 0.03 over 40°–70°N (boreal; Fig. 6f).

Within the boreal band from 60° to 70°N, tree cover fraction increased, primarily for boreal summergreen trees, anywhere from 0.05 to 0.60 in the RP runs, in association with surface warming. Across the Great Lakes Basin, Manchuria, and a band around 58°N from eastern Europe into western Russia, where the model favors grasses over trees owing to a large cold bias in

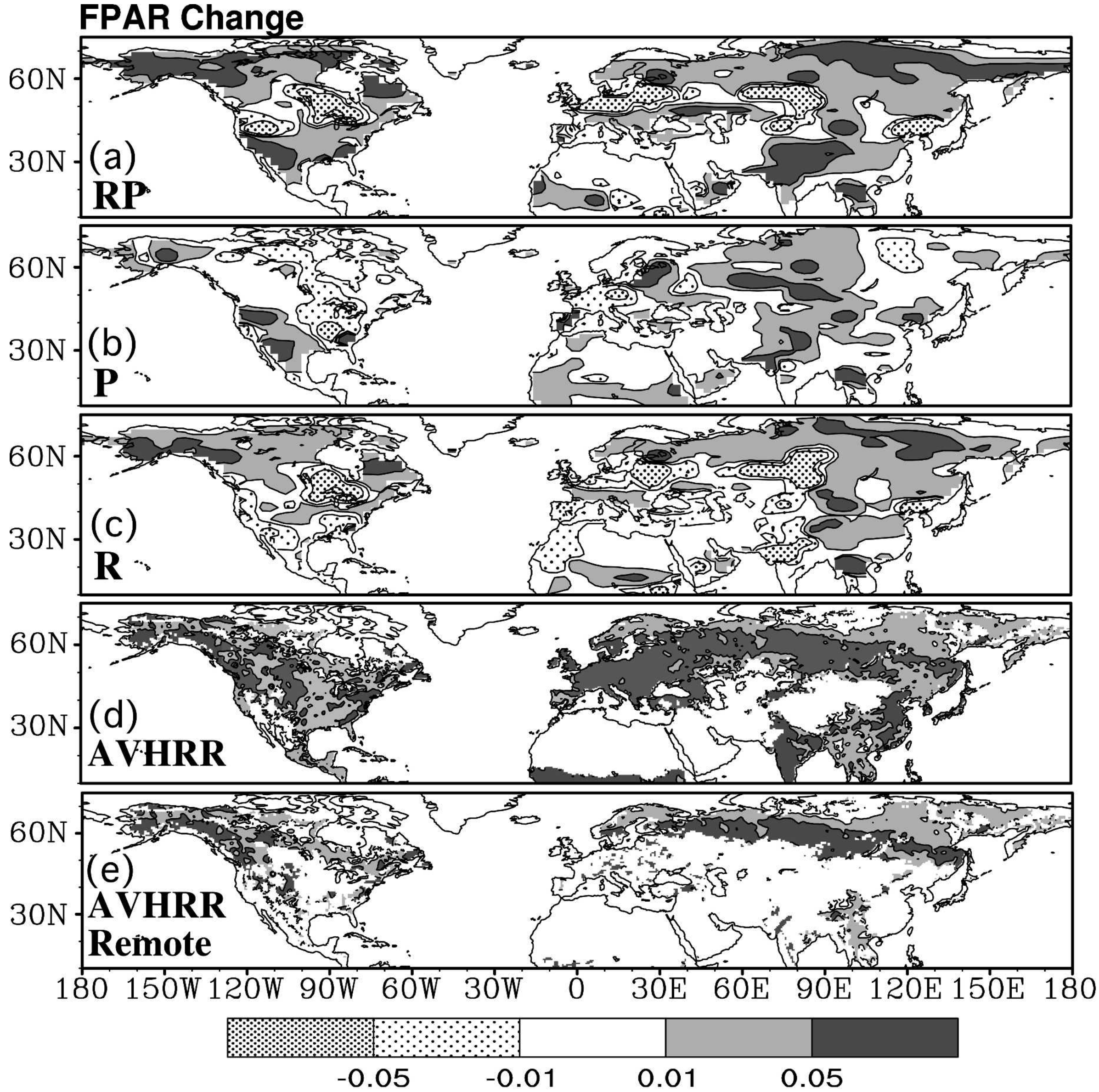

FIG. 9. Change in annual-average FPAR over 100 years from (a) RP run member 1, (b) the P run, and (c) the R run. (d) The change in annual-average FPAR from 1982 to 1999 based on Pathfinder AVHRR data (Myneni et al. 1997b). (e) As in (d) except regions that were anthropogenically altered by croplands and pastures are masked out, based on 1990 HYDE data (Goldewijk 2001).

winter and spring, the tree cover fraction decreased by 0.03–0.06 while FPAR also decreased by at least 0.05–0.10.

Trends in FPAR for runs RP, P, and R and Pathfinder observations are shown in Fig. 9. The primary changes in runs RP and R and the satellite data were a poleward expansion of the boreal forest (replacing tundra) and of tundra (replacing polar desert). The poleward advance of the boreal forest weakened the snow albedo feedback and increased the high-latitude warming as areas with deep snowpack once characterized by bare ground or grass developed tree cover; both the increase in tree canopy over the snowpack (Betts and Ball 1997) and the melting of snow cover resulted in reduced albedo. The 400-yr preindustrial control run of FOAM-LPJ revealed maximum high northern latitude variance in forest cover around 60°–70°N over Eurasia and Canada, the same zone where the boreal expansion in RP and R occurred. The AVHRR NDVI for 1981–2001 also exhibited strong variance within this zonal band. Despite this relatively high variance, the boreal expansion was statistically significant and persistent in both satellite data and model output. In the RP ensemble (Fig. 9a), FPAR increased at least by 0.04 ($P < 0.05$) within the boreal zone of 50°–70°N across Alaska, northern Canada, northern Eurasia, and China, primarily due to the radiative effect (Fig. 9c). FPAR trends in run P, shown in Fig. 9b, included increases over northern Mexico and the western United States, parts of central and northern Asia, and the Sahel, representing increased tree growth in predominantly low to moderately vegetated regions. Increasing levels of atmospheric CO_2 in the simulations led to reduced stomatal conductance, allowing plants to use water more efficiently and thus grow more effectively in drier climates.

Zhou et al. (2001) designed a persistence index for April–October average NDVI in order to identify regions where NDVI was persistently increasing during the satellite period. Their study found highly persistent increases in satellite-derived NDVI during 1982–99 extending from Europe, across north-central Russia, and into Mongolia, the southeast United States, and a band from Alaska through the U.S. Northern Plains. In the 100-yr RP runs, a similar index was applied using FPAR, which is highly related to NDVI (Sellers 1985; Tucker and Sellers 1986), and the findings were similar, including highly persistent increases over the band from Alaska into the Northern Plains, extending into the central and eastern United States, parts of Europe, and much of eastern Asia. In both the model and observations, peak Northern Hemisphere persistence trends were found around 60°N.

The observed trend in FPAR for 1982–99 is shown in Fig. 9d. In agreement with findings from Zhou et al. (2001), there was increased vegetation growth across much of North America and a band around 60°N through Eurasia, regions characterized by high vegetation seasonality and strong positive FPAR–emperature correlations in both model and satellite data. The expansion of vegetation cover reinforces the high-latitude warming trend, especially during spring, by replacing highly reflective snow-covered tundra with lower-albedo boreal forests (Robinson and Kukla 1985; Bonan et al. 1992; Laine and Heikinheimo 1996; Sharratt 1998). The largest observed FPAR increase, due to warming temperatures, was over Europe, particularly during springtime. In the RP ensemble, decreases in albedo during northern spring [March–May (MAM)] were most distinct within 60°–75°N, particularly over northern Asia and western Canada, reflecting the gradual decrease in snow cover and changeover from snow-covered tundra to boreal forest. In Fig. 9e, the 1990 HYDE land cover dataset was used to mask out anthropogenically altered regions of croplands and pastures in an attempt to isolate the remote FPAR trends. There is fairly good agreement between the FPAR trends in the RP runs and remote trends in AVHRR FPAR, both showing enhanced growth around 60°N across Alaska, Canada, and northern Eurasia. While the simulated changes in FPAR are similar in magnitude to those observed by satellite, the latter changes occur in just two decades, at a greater rate than those produced in the last two decades of the simulations.

The RP ensemble, in addition to a global decrease in evergreen tree cover, produces negative FPAR trends over several local midlatitude regions, including the Great Lakes Basin into Ontario, part of the U.S. Rockies, northern Europe, central Russia, and northeast China. These regional trends represent a radiatively induced decrease in boreal tree cover and increase in grass cover due to enhanced heat stress along the southern border of the simulated boreal forest, despite an increase in growing degree days. While the satellite data fails to exhibit a decrease in FPAR in most of these regions, the satellite record is limited to about two decades; these regions have also been altered by land use.

Nemani et al. (2003) applied a production efficiency model that incorporated satellite-derived vegetation and NCEP climate data for 1982–99 and calculated gridded annual NPP. They showed an increasing trend in NPP over the northern boreal forests, Amazon, and Congo, spatially comparable to the NPP trends in the RP ensemble. However, over the northern tundra and northern edge of the Asian boreal forest, Nemani et al. (2003) simulated a decreasing NPP trend due to cooling during the satellite period, while the 100-yr RP ensemble produced a positive trend representing boreal expansion. The cooling over the Eurasian tundra was also present in the second half of the twentieth century in the NCEP–NCAR reanalysis.

Several factors limit the ability of a GCM simulation with rising CO_2 levels to reproduce the greening trend from satellite data during the late twentieth century. The observed warming trend was briefly disrupted by the 1991 eruption of Mount Pinatubo (Parker et al. 1996), while aerosols have produced regional cooling over the eastern United States, Europe, and East Asia (Houghton et al. 1995, 2001). Many GCM simulations neglect the impact of volcanoes and increasing aerosol concentrations on climate. Almost one-fifth of the earth's land surface is covered by agriculture, replacing natural forests and grass. Trends in satellite-based NDVI include both climate changes and anthropogenic land use changes, so it is unlikely that a GCM excluding anthropogenic land use will accurately reproduce observed NDVI trends over many locations. However, an estimated 78% of the vegetation in the greening zone across Eurasia and North America within 40°–70°N is unmanaged (DeFries et al. 1998), so much of the NDVI trend there is likely linked to climate change. This region is also a more susceptible target area for model and observational comparisons. In addition, the positive trend in the North Atlantic Oscillation (NAO) index since the early 1970s might be responsible for much of Europe's warming (Hurrell 1995, 1996) and greening, while many GCMs, including FOAM-LPJ, fail to capture a positive NAO trend or its observed timing.

Nutrient supply limits forest growth over large regions, especially in the boreal forest where the nitrogen supply rate is restricted owing to slow decomposition of organic matter in the cold climate. Experiments by Oren et al. (2001) have shown that nutrient limitation can reduce the response of forest NPP to increasing CO_2. Nowak et al. (2004) summarize results from Free Air Carbon Dioxide Enrichment Experiments (FACE) including nutrient treatments. They find that the response of ecosystem NPP to CO_2 plus nutrient addition is greater than the response to CO_2 alone. However, the studies cited show that ecosystem NPP consistently responds to CO_2 increase, even in nutrient-limited ecosystems. Based on experiments involving six Arctic plant species, Oechel and Strain (1985) found that, after 22 months of exposure to high CO_2 levels, most plants showed an increase in photosynthesis. Two species in particular, deciduous shrubs and sedges, produced large increases in canopy photosynthesis rates at higher CO_2 and low nutrient supply. Because LPJ does not explicitly simulate nutrient cycling, the model likely overestimates the CO_2 effect to some degree. On the other hand, the response of simulated forest NPP to CO_2 enhancement in LPJ is broadly consistent with that observed in forest FACE studies (T. Hickler 2003, personal communication).

b. FPAR trend decomposition

Additional understanding of simulated annual FPAR trends was achieved by decomposing an area-average FPAR into four terms, each summed over the nine plant function types and all months:

$$\mathrm{FPAR} = \sum_{i=1}^{9} \overline{f}_i \overline{d}_i + \sum_{i=1}^{9} \overline{f}_i d'_i + \sum_{i=1}^{9} f'_i \overline{d}_i + \sum_{i=1}^{9} f'_i d'_i, \quad (1)$$

where f is vegetation cover fraction and d is seasonal leaf cover fraction for each of the nine plant function types. The first term on the right-hand side represents the 100-yr mean FPAR with no trend. A trend in the second term represents a change in leaf cover or length of the growing season (GDDs), while a trend in the third term involves changes in fractional vegetation cover. Trends in the fourth term, representing interactions or feedbacks between f and d, are found to be small.

The 30°–75°N average trend in FPAR in run RP was $+0.02$ century^{-1}. The vast majority (94%) of this increase was due to a widespread lengthening of the growing season, which increased leaf coverage ($d' > 0$). Within the high-latitude band of 60°–75°N, a larger FPAR trend of $+0.04$ century^{-1} was simulated in the RP ensemble, primarily due to an increase in deciduous tree cover and GDDs. The increase in vegetation cover ($f' > 0$ in term 3) was responsible for 56% of the FPAR trend, while the remaining 44% was associated with a positive trend in leaf coverage produced by greater GDDs (term 2). The positive FPAR trend in the northern boreal area was primarily due to a lengthening growing season, whereas in the northern tundra area it was mainly due to an increase in total vegetation cover.

The 30°–75°N mean FPAR trend in run R was weakly positive due to the near cancellation of a positive trend in term 2 and negative trend in term 3. Most of the area experienced an increase in GDDs due to radiative warming, resulting in a positive trend in term 2. However, term 3 showed a negative trend, with regional decreases in subtropical and midlatitude vegetation cover outweighing the broad high-latitude increases. Within 60°–75°N, the FPAR trend in run R was $+0.03$ century^{-1}, as a result of a combination of lengthening growing season (greater leaf coverage) and increasing vegetation cover. Finally, in run P, the small positive FPAR trend of $+0.01$ century^{-1} across 30°–75°N was almost entirely (95%) due to term 3, or a rise in vegetation cover. The general conclusion is that the positive FPAR trend across 30°–75°N in the RP ensemble was mostly due to an increase in the growing season owing to the radiative effect and an enhancement of vegetation cover by the physiological effect. Within 60°–75°N, the radiative effect contributed to an increase in GDD (leaf coverage) and vegetation cover, while the weaker physiological effect was limited to enhancing the mean vegetation cover.

c. Trends in tree ring width

Since the temporal extent of satellite-derived vegetation data is limited to two decades, this data cannot offer much insight into vegetation changes during the past two centuries. For the purpose of examining long-

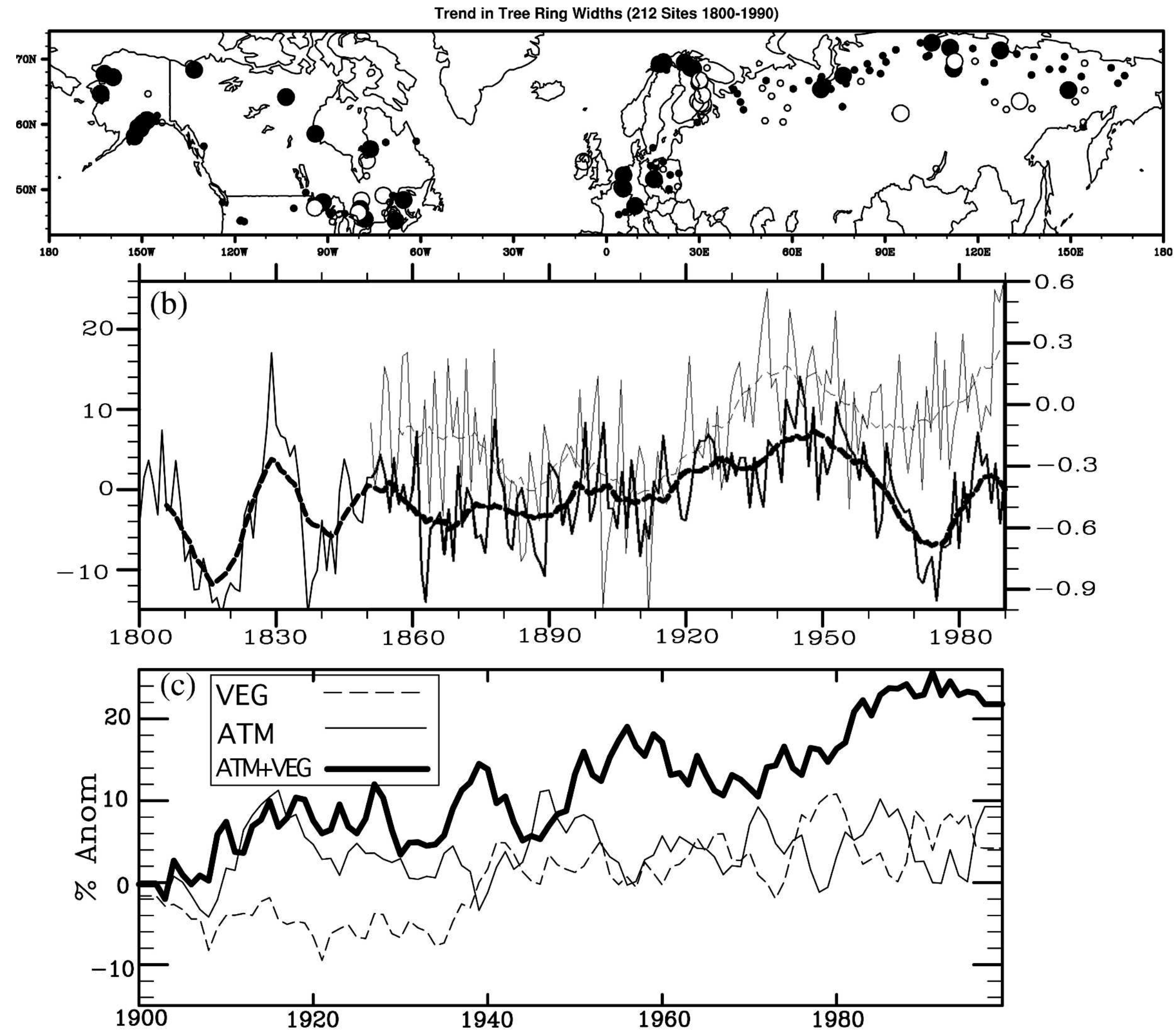

FIG. 10. (a) Location of 212 select tree ring data sites from the International Tree Ring Data Bank. Positive (negative) trends in tree ring width for 1800–1990 are shown as filled (hollow) circles, with significant trends of $P < 0.1$ identified as larger circles. (b) Time series of percent anomalies of average tree ring width from 212 sites for 1800–1999 (black line) and average Apr–Oct surface air temperature anomalies (°C) for 45°–75°N from CRU data (Jones and Moberg 2003) (gray line). (c) Time series of simulated percent anomalies of tree ring width vs first five years, for 45°–75°N.

term vegetation growth in the model, standardized tree ring width data for 212 sites within 45°–75°N were analyzed for 1800–1999 and related to model trends. Figure 10 presents the position and tree ring width trends of each site and time series of average ring width and CRU temperature anomalies for April–October for the same latitudinal band. During the first few decades of the 1800s, for which data availability is limited, the average ring width showed strong decadal variability. During 1860–1950, a gradual but persistent increase in ring width produced a net rise in growth of 12.2%, similar to findings of Briffa et al. (1998). Briffa et al. (1998) also found a decrease in ring width and maximum latewood density since 1950, despite a general warming, and proposed a possible link to increased UV radiation, due to the ozone hole. Perhaps this decrease in growth could partly be attributed to the earlier April–October cooling during the 1940s and 1950s (Fig. 10).

Within 60°–75°N, 91 out of 130 sites (70%) showed a positive trend in tree ring width during 1800–1990. Over Alaska and northern Canada, positive trends dominated and were mostly significant at $P < 0.1$. Over Eurasia, many sites along the Arctic Circle exhibited a positive trend, while a number of sites a few degrees equatorward showed negative trends, suggesting a poleward shift in favorable growing conditions. The observed increase in tree growth at northern high latitudes was also simulated by the RP ensemble.

Briffa et al. (1998) and Hughes (2000) further noted that tree ring records have shown increasing growth beginning in the mid-nineteenth century, decades before the strong warming trend of the early twentieth century. These authors suggested that the physiological effect of early rising CO_2 might have played a role in the enhanced growth. For instance, during 1860–1910, April–October mean temperature for 45°–75°N slightly decreased while the mean ring width gradually increased. The CO_2 level rose by 26 ppm from 1850 to 1950 and 58 ppm from 1950 to 2000, with the latter period's rate of increase being about four times that of the former period. LaMarche et al. (1984) attributed the increasing growth rates of subalpine conifers in the western United States since the mid-nineteenth century to the physiological effect, noting the continual increase since 1960 despite cooling.

It is suggested here that the average tree-ring width increase might have been due to the physiological effect of increasing CO_2 until about 1910 and perhaps a combination of physiological and radiative warming after 1910. The strong warming trends seen in the CRU data during 1910–40, and since 1970, contributed to larger ring width growth. The period of 1881–1960 demonstrated a strong positive correlation of 0.40 between the mean ring width and April–October temperature; this correlation reached +0.65 when the ring width for each year was compared with the average annual temperature for that year and the three years prior. When the data were divided into five regions (Alaska, Russia, Canada, Europe, and the northern United States), the positive trend in ring width from the mid-nineteenth to mid-twentieth centuries was most distinct in Alaska (+4.4 mm century^{-1}) and least so over the northern United States (+0.4 mm century^{-1}).

Mean annual stem diameter increment was computed during the model simulations to represent ring width growth. Simulated mean ring width increased 22% in the first 100-yr RP simulation averaged over the land within 45°–75°N (Fig. 10c). The simulated ring width growth, however, increased at a much greater rate than observed. While tree ring measurements are typically limited to mature trees, the average growth rate in the model would also consider saplings, with potentially large percent growth rates. Larger simulated warming than observed within 45°–75°N, along with the absence of simulated widespread decadal cold periods, likely contributed to the enhanced tree ring growth. It is also possible that FOAM-LPJ overestimated the physiological forcing on vegetation growth rate into the northern tundra. Within the R and P simulations, the percent increases in mean ring width were 4% and 14%, respectively, emphasizing the role of the physiological forcing in enhancing mid-high-latitude growth. The physiological effect was the dominant forcing globally and produced relatively large positive trends in tree growth over the Congo, Amazon, Southeast Asia, northern Australia, and the central and eastern United States. The radiative effect reduced tree growth within the Tropics and subtropics due to a drying trend, while slightly enhancing growth over parts of Canada and eastern Asia (simulated tropical ring width growth pertains to "virtual" ring widths). The trends are not well known for the Tropics because most tropical trees lack distinct annual rings. However, an increasing trend in tropical tree growth rates has been inferred from direct measurements (Phillips and Gentry 1994) and attributed to the physiological effect of increasing CO_2.

6. Conclusions

Observed climate change signatures have included a global warming trend, strongest at the high latitudes (Hansen et al. 1999); a decrease in Northern Hemispheric snow cover (Groisman et al. 1994); and increasing atmospheric water vapor in the Tropics (Houghton et al. 1995). The ecological consequences of these changes have included a global greening and a strong greening and poleward expansion of the Eurasian and North American boreal forests. Satellite imagery has been the primary evidence of these vegetation changes but is limited to only two decades of temporal recording. In addition, the observed climate and vegetation records contain signatures of the effects of anthropogenic land use and aerosols, making it difficult to determine the specific impact of rising carbon dioxide levels and climate change.

A fully coupled atmosphere–ocean–land surface model with dynamic vegetation has been used here to simulate changes in climate and vegetation due to rising CO_2 from preindustrial to modern times, as well as to diagnose the separate radiative and physiological effects. The model reproduced broad aspects of the natural (excluding land use) biome distribution as well as seasonal shifts in vegetation, despite overprediction of forest in many areas and an excessive simulated area of polar desert. Despite its biases, the fully coupled model represents an advance compared with models of intermediate complexity (e.g., Brovkin et al. 2002) in simulating a wide range of feedbacks among the atmosphere, biosphere, ocean, and cryosphere, including biogeophysical feedbacks associated with the effects of CO_2 on plant physiology.

FOAM-LPJ simulations with rising CO_2 produced a general global warming, strongest at high latitudes. The overall global warming from preindustrial to modern times was greater in the model than observed; this can likely be attributed to the absence of aerosols, volcanoes, and anthropogenic land use in the model and an overactive hydrological cycle. The model's cold bias probably enhanced the role of albedo feedback during the simulations and resulted in greater positive temperature trends. The overall trend (1900–2000) in global annual mean temperature was additive ($RP = R + P$) and dominated by the radiative forcing, with only a small impact found for the physiological effect. However, the physiological effect on DJF temperature was not negligible, resulting in significant warming over northern Europe and central and eastern Asia, associated with an extended growing season and enhanced wintertime FPAR. Spatially, the warming was not additive ($RP \neq R + P$) at mid and high latitudes, particularly during winter. Both the RP ensemble and 1901–2000 CRU data showed a 3% rise in global land surface precipitation.

The model simulated a global greening trend, which included a poleward expansion of the Eurasian and North American boreal forest and an expansion of tundra into the northern polar desert. The persistence of vegetation growth across unmanaged boreal latitudes agreed reasonably well with the findings of Zhou et al. (2001). The simulations suggest that, from preindustrial to modern times, the increase in global total tree cover and vegetation was primarily due to the physiological impact of rising CO_2 on plant growth, with positive trends noted even within the first couple of decades of run P. The positive FPAR trend across 30°–75°N in the RP ensemble resulted from a lengthening of the growing season due to the radiative effect and an enhancement of vegetation cover due the physiological effect. Both the radiative and physiological runs simulated increased growth of boreal summergreen trees, suggesting that this part of the boreal greening was due to a combination of both effects. The radiative effect supports boreal expansion by expanding the growing season and melting snow cover at high latitudes. The physiological effect in run P accelerated the northern high-latitude expansion by enhancing forest growth in ecological transition regions, where both trees and grass coexist, through CO_2 fertilization.

Hughes (2000) proposed that the physiological effect of CO_2 might have played a role in enhancing vegetation growth as far back as the beginning of the mid-nineteenth century, prior to the twentieth-century warming. During 1860–1950, Northern Hemisphere tree ring widths at mid and high latitudes increased linearly, even during the 1860–1910 cooling period (Briffa et al. 1998). Potentially, the physiological effect may have enhanced vegetation growth prior to 1910, despite the small rise in CO_2, while a combination of warming and the physiological effect may have acted throughout most of the twentieth century. The RP ensemble of simulations produced a northern mid- to high-latitude increase in tree ring width, primarily due to the physiological CO_2 effect.

It is possible that biases within FOAM-LPJ could have impacted the results of these preindustrial to modern transient simulations, which were performed without flux adjustment. For example, FOAM's overactive hydrological cycle might amplify its sensitivity to rising levels of greenhouse gases. However, the resulting overabundance of vegetation cover might limit the physiological response of vegetation to carbon fertilization as the physiological response is usually greatest in low to moderately vegetated regions with limited water resources. As model development progresses, it is expected that biases will be reduced.

Acknowledgments. This research was funded by DOE and NSF. The authors thank Dr. Navin Ramankutty and Dr. Christine Delire (SAGE) for their insight on vegetation–climate interaction, Dr. Waltraud Brinkmann (University of Wisconsin—Madison's Department of Geography) for her advice on tree ring data, Dr. Benjamin Smith (University of Lund, Sweden) for suggestions involving LPJ code, and both Pat Behling and Mark Marohl (CCR) for assistance with figure preparation. Thanks also to two anonymous reviewers for their suggestions.

REFERENCES

Bergengren, J. C., S. L. Thompson, D. Pollard, and R. M. Deconto, 2001: Modeling global climate–vegetation interactions in a doubled CO_2 world. *Climate Change,* **50,** 31–75.

Betts, A. K., and J. H. Ball, 1997: Albedo over the boreal forest. *J. Geophys. Res.,* **102,** 28 901–28 909.

Betts, R. A., P. M. Cox, S. E. Lee, and F. I. Woodward, 1997: Contrasting physiological and structural vegetation feedbacks in climate change simulations. *Nature,* **387,** 796–799.

——, ——, M. Collins, P. Harris, C. Huntingford, and C. D. Jones, 2004: The role of ecosystem–atmosphere interactions in simulated Amazonian precipitation decrease and forest dieback under global warming. *Theor. Appl. Climatol.,* **78,** 157–175.

Bonan, G. B., D. Pollard, and S. L. Thompson, 1992: Effects of boreal forest vegetation on global climate. *Nature,* **359,** 716–718.

Bounoua, L., and Coauthors, 1999: Interactions between vegetation and climate: Radiative and physiological effects of doubled atmospheric CO_2. *J. Climate,* **12,** 309–324.

Briffa, K. R., F. H. Schweingruber, P. D. Jones, T. J. Osborn, I. C. Harris, S. G. Shiyatov, E. A. Vaganov, and H. Grudd, 1998: Trees tell of past climates: But are they speaking less clearly today? *Philos. Trans. Roy. Soc. London,* **353B,** 65–73.

Brovkin, V., J. Bendtsen, M. Claussen, A. Ganopolski, C. Kubatzki, V. Petoukhov, and A. Andreev, 2002: Carbon cycle, vegetation, and climate dynamics in the Holocene with the CLIMBER-2 model. *Global Biogeochem. Cycles,* **16,** 1–20.

——, S. Levis, M.-F. Loutre, M. Crucifix, M. Claussen, A. Ganopolski, C. Kubatzki, and V. Petoukhov, 2003: Stability analysis of the climate–vegetation system in the northern high latitudes. *Climate Change,* **57,** 119–138.

Chase, T. N., R. A. Pielke Sr., T. G. G. Kittel, M. Zhao, A. J. Pitman, S. W. Running, and R. R. Nemani, 2001: Relative climatic effects of landcover change and elevated carbon dioxide combined with aerosols: A comparison of model results and observations. *J. Geophys. Res.,* **106,** 31 685–31 691.

Claussen, M., 1994: Coupling global biome models with climate models. *Climate Res.,* **4,** 203–221.

——, and M. Esch, 1994: Biomes computed from simulated climatologies. *Climate Dyn.,* **9** (4–5), 235–243.

Cramer, B. A., and Coauthors, 2001: Global response of terrestrial ecosystem structure and function to CO_2 and climate change: Results from six dynamic global vegetation models. *Global Change Biol.,* **7,** 357–373.

D'Arrigo, R., G. C. Jacoby, and I. Y. Fung, 1987: Boreal forests and atmosphere–biosphere exchange of carbon dioxide. *Nature,* **329,** 321–323.

DeFries, R. S., M. Hansen, J. Townshend, and R. Sohlberg, 1998: Global land cover classification at 8km spatial resolution: The use of training data derived from LANDSAT imagery in decision tree classifiers. *Int. J. Remote Sens.,* **19,** 3141–3168.

——, J. R. G. Townshend, and M. C. Hansen, 1999: Continuous fields of vegetation characteristics at the global scale at 1 km resolution. *J. Geophys. Res.,* **104,** 16 911–16 925.

——, M. C. Hansen, J. R. G. Townshend, A. C. Janetos, and T. R. Loveland, 2000: A new global 1-km dataset of percentage tree cover derived from remote sensing. *Global Change Biol.,* **6,** 247–254.

Drake, J., I. Foster, J. Michalakes, B. Toonen, and P. Worley, 1995: Design and performance of a scalable parallel community climate model. *Parallel Comput.,* **21,** 1571–1591.

Easterling, D. R., T. R. Karl, and K. P. Gallo, 2000: Observed climate variability and change of relevance to the biosphere. *J. Geophys. Res.,* **105,** 20 101–20 114.

Fanning, A. F., and A. J. Weaver, 1997: On the role of flux adjustments in an idealised coupled climate model. *Climate Dyn.,* **13,** 691–701.

Fung, I., 1997: A greener north. *Nature,* **386,** 659–660.

Ganopolski, A., C. Kubatzki, M. Claussen, V. Brovkin, and V. Petoukhov, 1998: The influence of vegetation–atmosphere–ocean interaction on climate during the mid-Holocene. *Science,* **280,** 1916–1919.

Goldewijk, K. K., 2001: Estimating global land use change over the past 300 years: The HYDE database. *Global Biogeochem. Cycles,* **15,** 417–433.

Graumlich, L. J., 1991: Subalpine tree growth, climate, and increasing CO_2: An assessment of recent growth trends. *Ecology,* **72,** 1–11.

Gregory, J. M., and J. F. B. Mitchell, 1997: The climate response to CO_2 of the Hadley Centre coupled AOGCM with and without flux adjustment. *Geophys. Res. Lett.,* **24,** 1943–1946.

Groisman, P. Y., T. R. Karl, R. W. Knight, and G. L. Stenchinkov, 1994: Changes of snow cover, temperature, and radiative heat balance over the Northern Hemisphere. *J. Climate,* **7,** 1633–1656.

Hansen, J. E., R. Ruedy, J. Glascoe, and M. Sato, 1999: GISS analysis of surface temperature change. *J. Geophys. Res.,* **104,** 30 997–31 022.

Harrison, S. P., J. E. Kutzbach, Z. Liu, P. J. Bartlein, B. Otto-Bliesner, D. Muhs, I. C. Prentice, and R. S. Thompson, 2003: Mid-Holocene climates of the Americas: A dynamical response to changed seasonality. *Climate Dyn.,* **20,** 663–688.

Houghton, J. T., L. G. Meira Filho, B. A. Callander, N. Harris, A. Kattenberg, and K. Maskell, Eds., 1995: *Climate Change 1995: The Science of Climate Change.* Cambridge University Press, 572 pp.

——, Y. Ding, D. J. Griggs, M. Noguer, P. J. van der Linden, X. Dai, K. Maskell, and C. A. Johnson, Eds, 2001: *Climate Change 2001: The Scientific Basis*. Cambridge University Press, 881 pp.

Hughes, L., 2000: Biological consequences of global warming: Is the signal already apparent? *Trends Ecol. Evol.,* **15,** 56–61.

Hurrell, J. W., 1995: Decadal trends in the North Atlantic Oscillation: Regional temperatures and precipitation. *Science,* **269,** 676–679.

——, 1996: Influence of variations in extratropical wintertime teleconnections on Northern Hemisphere temperature. *Geophys. Res. Lett.,* **23,** 665–668.

Jacob, R., 1997: Low frequency variability in a simulated atmosphere ocean system. Ph.D. thesis, University of Wisconsin—Madison, 159 pp.

——, C. Schafer, I. Foster, M. Tobis, and J. Anderson, 2001: Computational design and performance of the Fast Ocean Atmosphere Model, Version One. *Proceedings of the 2001 International Conference on Computational Science,* V. N. Alexandrov, J. J. Dongarra, and C. J. K. Tan, Eds., Springer-Verlag, 175–184.

Jones, P. D., and A. Moberg, 2003: Hemispheric and large-scale surface air temperature variations: An extensive revision and an update to 2001. *J. Climate,* **16,** 206–223.

Joos, F., S. Gerber, I. C. Prentice, B. L. Otto-Bliesner, and P. J. Valdes, 2004: Transient simulations of Holocene atmospheric carbon dioxide and terrestrial carbon since the Last Glacial Maximum. *Global Biogeochem. Cycles,* **18,** GB2002, doi:10.1029/2003GB002156.

Kalnay, E., and Coauthors, 1996: The NCEP/NCAR 40-Year Reanalysis Project. *Bull. Amer. Meteor. Soc.,* **77,** 437–471.

Kaplan, J. O., and Coauthors, 2003: Climate change and arctic ecosystems. II: Modeling, paleodata–model comparisons, and future projections. *J. Geophys. Res.,* **108,** 8171, doi:10.1029/2002JD002559.

Kicklighter, D. W., and Coauthors, 1999: A first-order analysis of the potential role of CO_2 fertilization to affect the global carbon budget: A comparison of four terrestrial biosphere models. *Tellus,* **51B,** 343–366.

Kiehl, J. T., J. J. Hack, G. B. Bonan, B. A. Boville, D. L. Williamson, and P. J. Rasch, 1998: The National Center for Atmospheric Research Community Climate Model: CCM3. *J. Climate,* **11,** 1131–1150.

Laine, V., and M. Heikinheimo, 1996: Estimation of surface albedo from NOAA AVHRR data in high latitudes. *Tellus,* **48A,** 424–441.

LaMarche, V. C., D. A. Graybill, H. C. Fritts, and M. R. Rose, 1984: Increasing atmospheric carbon dioxide: Tree ring evidence for growth enhancement in natural vegetation. *Science,* **225,** 1019–1021.

Levis, S., J. A. Foley, and D. Pollard, 2000: Large-scale vegetation feedbacks on a doubled CO_2 climate. *J. Climate,* **13,** 1313–1325.

Los, S. O., and Coauthors, 2000: A global 9-yr biophysical land surface dataset from NOAA AVHRR data. *J. Hydrometeor.,* **1,** 183–199.

Lucht, W., and Coauthors, 2002: Climatic control of the high-latitude vegetation greening trend and Pinatubo effect. *Science,* **296,** 1687–1689.

McCarthy, J., O. Canziani, N. Leary, D. Dokken, and K. White, Eds., 2001: *Climate Change 2001: Impacts, Adaptation, and Vulnerability.* Cambridge University Press, 1032 pp.

McGuire, A. D., and Coauthors, 2001: Carbon balance of the terrestrial biosphere in the twentieth century: Analyses of CO_2, climate and land use effects with four process-based ecosystem models. *Global Biogeochem. Cycles,* **15,** 183–206.

Meehl, G. A., W. M. Washington, T. M. L. Wigley, J. M. Arblaster, and A. Dai, 2003: Solar and greenhouse gas forcing and climate response in the twentieth century. *J. Climate,* **16,** 426–444.

Myneni, R. B., C. D. Keeling, C. J. Tucker, G. Asrar, and R. R. Nemani, 1997a: Increased plant growth in the northern high latitudes from 1981–1991. *Nature,* **386,** 698–701.

——, R. R. Nemani, and S. W. Running, 1997b: Estimation of global leaf area index and absorbed par using radiative transfer models. *IEEE Trans. Geosci. Remote Sens.,* **35,** 1380–1393.

Nemani, R. R., C. D. Keeling, H. Hashimoto, W. M. Jolly, S. C. Piper, C. J. Tucker, R. B. Myneni, and S. W. Running, 2003: Climate-driven increases in global terrestrial net primary production from 1982 to 1999. *Science,* **300,** 1560–1563.

NOAA, 1997: Contributors of the International Tree-Ring Data Bank. IGBP PAGES/World Data Center for Paleoclimatology, NOAA/NGDC Paleoclimatology Program, Boulder, Colorado. [Available online at http://ngdc.noaa.gov.]

Nowak, R. S., D. S. Ellsworth, and S. D. Smith, 2004: Tansley Review: Functional responses of plants to elevated atmospheric CO_2—Do photosynthetic and productivity data from FACE experiments support early predictions? *New Phytol.,* **162,** 253–280.

Oechel, W. C., and B. R. Strain, 1985: Native species responses to increased atmospheric carbon dioxide concentration. *Direct Effects of Increasing Carbon Dioxide on Vegetation,* B. R. Strain and J. D. Cure, Eds., U.S. Dept. of Energy Rep. DOE/ER-0238, 286 pp.

Oren, R., and Coauthors, 2001: Soil fertility limits carbon sequestration by forest ecosystems in a CO_2-enriched atmosphere. *Nature,* **411,** 469–472.

Parker, D. E., H. Wilson, P. D. Jones, J. Christy, and C. K. Folland, 1996: The impact of Mount Pinatubo on climate. *Int. J. Climatol.,* **16,** 487–497.

Parmesan, C., and G. Yohe, 2003: A globally coherent fingerprint of climate change impacts across natural systems. *Nature,* **421,** 37–42.

Phillips, O. L., and A. H. Gentry, 1994: Increasing turnover through time in tropical forests. *Science,* **263,** 954–958.

Prentice, I. C., and M. T. Sykes, 1995: Vegetation geography and carbon storage changes. *Biotic Feedbacks in the Global Climate System*, G. M. Woodwell and F. T. Mackenzie, Eds., Oxford University Press, 304–312.

Ramankutty, N., and J. A. Foley, 1999: Estimating historical changes in global land cover: Croplands from 1700 to 1992. *Global Biogeochem. Cycles,* **13,** 997–1027.

Reynolds, R. W., and T. M. Smith, 1994: Improved global sea surface temperature analyses. *J. Climate,* **7,** 929–948.

Robinson, D. A., and G. Kukla, 1985: Maximum surface albedo of seasonally snow-covered lands in the Northern Hemisphere. *J. Climate Appl. Meteor.,* **24,** 402–411.

Sellers, P. J., 1985: Canopy reflectance, photosynthesis, and transpiration. *Int. J. Remote Sens.,* **6,** 1335–1372.

——, and Coauthors, 1996: Comparison of radiative and physiological effects of doubled atmospheric CO_2 on climate. *Science,* **271,** 1402–1406.

Sharratt, B. S., 1998: Radiative exchange, near-surface temperature and soil water of forest and cropland in interior Alaska. *Agric. For. Meteor.,* **89,** 269–280.

Sitch, S., 2000: The role of vegetation dynamics in the control of atmospheric CO_2 content. Ph.D. dissertation, Lund University, 213 pp.

——, and Coauthors, 2003: Evaluation of ecosystem dynamics, plant geography and terrestrial carbon cycling in the LPJ dynamic global vegetation model. *Global Change Biol.,* **9,** 161–185.

Smith, T. M., and R. W. Reynolds, 2003: Extended reconstruction of global sea surface temperatures based on COADS data (1854–1997). *J. Climate,* **16,** 1495–1510.

——, ——, R. E. Livesey, and D. C. Stokes, 1996: Reconstruction of historical sea surface temperature using empirical orthogonal functions. *J. Climate,* **9,** 1403–1420.

Solomon, A. M., K. C. Prentice, R. Leemans, and W. P. Cramer, 1993: The interaction of climate and land use in future terrestrial carbon storage and release. *Water Air Soil Pollut.,* **70,** 595–614.

Stott, P. A., S. F. B. Tett, G. S. Jones, M. R. Allen, J. F. B. Mitchell, and G. J. Jenkins, 2000: External control of 20th century temperature by natural and anthropogenic forcings. *Science,* **290,** 2133–2137.

——, ——, ——, ——, W. J. Ingram, and J. F. B. Mitchell, 2001: Attribution of twentieth century temperature change to natural and anthropogenic causes. *Climate Dyn.,* **17,** 1–22.

Tett, S. F. B., and Coauthors, 2000: Estimation of natural and anthropogenic contributions to 20th century. Hadley Centre Tech. Note 19, 52 pp.

Tucker, C. J., and P. J. Sellers, 1986: Satellite remote sensing of primary production. *Int. J. Remote Sens.,* **7,** 1395–1416.

——, D. A. Slayback, J. E. Pinzon, S. O. Los, R. B. Myneni, and M. G. Taylor, 2001: Higher northern latitude NDVI and growing season trends from 1982 to 1999. *Int. J. Biometeor.,* **45,** 184–190.

Willmott, C. J., and K. Matsuura, 2000: Terrestrial air temperature and precipitation: Monthly and annual time series (1950–1996) (Version 1.01). [Available online at http://climate.geog.udel.edu/~climate/html_pages/README.ghcn_ts.html.]

Wu, L., Z. Liu, and R. Gallimore, 2003: Pacific decadal variability: The tropical Pacific mode and North Pacific mode. *J. Climate,* **16,** 1101–1120.

Xie, P., and P. A. Arkin, 1996: Analyses of global monthly precipitation using gauge observations, satellite estimates, and numerical model predictions. *J. Climate,* **9,** 840–858.

——, and ——, 1997: Global precipitation: A 17-year monthly analysis based on gauge observations, satellite estimates, and numerical model outputs. *Bull. Amer. Meteor. Soc.,* **78,** 2539–2558.

Zhou, L., C. J. Tucker, R. K. Kaufmann, D. Slayback, N. V. Shabanov, and R. B. Myneni, 2001: Variations in northern vegetation activity inferred from satellite data of vegetation index during 1981 to 1999. *J. Geophys. Res.,* **106,** 20 069–20 083.

——, R. K. Kaufmann, Y. Tian, R. B. Myneni, and C. J. Tucker, 2003: Relation between interannual variations in satellite measures of northern forest greenness and climate between 1982 and 1999. *J. Geophys. Res.,* **108,** 4004, doi:10.1029/2002JD002510.